

**AFRL-AFOSR-UK-TR-2012-0036**



**An Integrated Experimental and Computational Study of  
Heating due to Surface Catalysis under Hypersonic  
Conditions**

**Professor Olivier P. Chazot**

**Institut Von Karman De Dynamique Des Fluides  
Aeronautics and Aerospace Department  
Waterloosesteenweg 72  
Rhode-Saint-Genese, Belgium B-1640**

EOARD Grant 11-3066

Report Date: August 2012

Final Report from 25 August 2011 to 24 February 2012

**Distribution Statement A: Approved for public release distribution is unlimited.**

**Air Force Research Laboratory  
Air Force Office of Scientific Research  
European Office of Aerospace Research and Development  
Unit 4515 Box 14, APO AE 09421**

<b>REPORT DOCUMENTATION PAGE</b>				Form Approved OMB No. 0704-0188	
<small>Public reporting burden for this collection of information is estimated to average 1 hour per response, including the time for reviewing instructions, searching existing data sources, gathering and maintaining the data needed, and completing and reviewing the collection of information. Send comments regarding this burden estimate or any other aspect of this collection of information, including suggestions for reducing the burden, to Department of Defense, Washington Headquarters Services, Directorate for Information Operations and Reports (0704-0188), 1215 Jefferson Davis Highway, Suite 1204, Arlington, VA 22202-4302. Respondents should be aware that notwithstanding any other provision of law, no person shall be subject to any penalty for failing to comply with a collection of information if it does not display a currently valid OMB control number.</small> <b>PLEASE DO NOT RETURN YOUR FORM TO THE ABOVE ADDRESS.</b>					
<b>1. REPORT DATE (DD-MM-YYYY)</b> 22 August 2012		<b>2. REPORT TYPE</b> Final Report		<b>3. DATES COVERED (From – To)</b> 25 August 2011 – 24 February 2012	
<b>4. TITLE AND SUBTITLE</b>  <b>An Integrated Experimental and Computational Study of Heating due to Surface Catalysis under Hypersonic Conditions</b>				<b>5a. CONTRACT NUMBER</b>  FA8655-11-1-3066	
				<b>5b. GRANT NUMBER</b>  Grant 11-3066	
				<b>5c. PROGRAM ELEMENT NUMBER</b>  61102F	
				<b>5d. PROJECT NUMBER</b>	
<b>6. AUTHOR(S)</b>  Professor Olivier P. Chazot				<b>5d. TASK NUMBER</b>	
				<b>5e. WORK UNIT NUMBER</b>	
<b>7. PERFORMING ORGANIZATION NAME(S) AND ADDRESS(ES)</b> Institut Von Karman De Dynamique Des Fluides Aeronautics and Aerospace Department Waterlooosesteenweg 72 Rhode-Saint-Genese, Belgium B-1640				<b>8. PERFORMING ORGANIZATION REPORT NUMBER</b>  N/A	
<b>9. SPONSORING/MONITORING AGENCY NAME(S) AND ADDRESS(ES)</b>  EOARD Unit 4515 BOX 14 APO AE 09421				<b>10. SPONSOR/MONITOR'S ACRONYM(S)</b>  AFRL/AFOSR/RSW (EOARD)	
				<b>11. SPONSOR/MONITOR'S REPORT NUMBER(S)</b>  AFRL-AFOSR-UK-TR-2012-0036	
<b>12. DISTRIBUTION/AVAILABILITY STATEMENT</b>  Approved for public release; distribution is unlimited. (approval given by local Public Affairs Office)					
<b>13. SUPPLEMENTARY NOTES</b>					
<b>14. ABSTRACT</b>  This report details the collaboration between the University of Minnesota and the Von Karman Institute. There were two main goals to this collaborative project: (1) To use the US3D code to validate the LHTS approach employed by VKI. Since LHTS is a very useful and widely used technique used to interpret ICP data, a better understanding of its accuracy and potential limitations would be a valuable contribution. (2) To use the US3D code to directly interpret ICP data and thereby develop new high-fidelity models for high-temperature gas-surface interactions.  This report details the collaboration which occurred August 2011 – February 2012					
<b>15. SUBJECT TERMS</b>  EOARD, ablation, Aerodynamics, Hypersonics					
<b>16. SECURITY CLASSIFICATION OF:</b>			<b>17. LIMITATION OF ABSTRACT</b>  SAR	<b>18. NUMBER OF PAGES</b>  40	<b>19a. NAME OF RESPONSIBLE PERSON</b> Gregg Abate
<b>a. REPORT</b> UNCLAS	<b>b. ABSTRACT</b> UNCLAS	<b>c. THIS PAGE</b> UNCLAS			<b>19b. TELEPHONE NUMBER</b> (Include area code) +44 (0)1895 616021

# An Integrated Experimental and Computational Study of Heating due to Surface Catalysis under Hypersonic Conditions

EOARD Award N°. FA8655-11-1-3066

O. Chazot<sup>\*</sup>, T. Schwartzentruber<sup>\*\*</sup>, A. Lani<sup>\*</sup>, N. Villedieu<sup>\*</sup> and P. Barbante<sup>\*\*\*</sup>

<sup>\*</sup>Von Karman Institute, Aeronautics & Aerospace Dept.

<sup>\*\*</sup>Aerospace Engineering & Mechanics, University of Minnesota

<sup>\*\*\*</sup>Politecnico di Milano, Dept. of Mathematics

# Contents

<b>I Computational Modeling of the VKI Inductively Coupled Plasma (ICP) Facility with the Minnesota US3D Code</b>	<b>4</b>
<b>1 Motivation</b>	<b>4</b>
<b>2 Project Accomplishments</b>	<b>5</b>
2.1 Grid convergence and US3D numerics for simple subsonic flows . . . . .	6
2.2 Comparison of 2D vs. 3D simulations . . . . .	7
2.3 Subsonic Outflow and Plasma Jet Inflow Boundary Conditions . . . . .	8
2.4 VKI LTE vs US3D solution comparisons . . . . .	9
<b>3 Future Work</b>	<b>15</b>
 <b>II Numerical simulation of plasma jet and gas-surface interaction around blunted plate with COOLFluid</b>	 <b>16</b>
0.1 COOLFluid platform . . . . .	16
<b>1 Physical modeling</b>	<b>17</b>
1.1 Park's 2-temperature model . . . . .	17
1.1.1 Mass production / destruction terms . . . . .	18
1.1.2 Energy exchange terms . . . . .	19
1.2 Modeling of ICP facility . . . . .	19
1.2.1 Electromagnetic field equations . . . . .	20
1.2.2 Coupled system . . . . .	20
<b>2 Numerical method</b>	<b>21</b>
2.1 Space discretization . . . . .	21
2.1.1 AUSM+ scheme . . . . .	22
2.1.2 Discretization of diffusive Fluxes . . . . .	22
2.1.3 Discretization of source Terms . . . . .	23
2.1.4 Boundary conditions for nonequilibrium solver . . . . .	24
2.1.5 Boundary conditions for ICP solver . . . . .	25
2.1.6 Implicit time integration . . . . .	26
<b>3 Numerical results</b>	<b>26</b>
3.1 ICP simulation . . . . .	26
3.2 Nonequilibrium simulation . . . . .	27

<b>III Numerical simulation of plasma jet around the VKI rounded nose flat plate probe</b>	<b>31</b>
<b>1 Introduction</b>	<b>31</b>
<b>2 Numerical model</b>	<b>32</b>
2.1 Boundary conditions . . . . .	32
<b>3 Results</b>	<b>33</b>

## Part I

# Computational Modeling of the VKI Inductively Coupled Plasma (ICP) Facility with the Minnesota US3D Code

## 1 Motivation

The US3D code developed at the University of Minnesota in Prof. Graham Candler's research group has gained widespread use throughout NASA and U.S. Air Force research laboratories. It is a state-of-the-art flow solver for challenging hypersonic flows and has been validated with high enthalpy shock tunnel experiments (CUBRC and Caltech tunnels for example) as well as with flight data for over a decade. This work has been extremely successful and the next major challenge is to develop new finite rate gas-surface interaction models and incorporate them into the US3D code. This would enable high-fidelity solutions to flows involving surface catalysis and ablation; problems of increasing importance to the USAF. Recently, Prof. Thomas Schwartzentrubers group at the University of Minnesota implemented a Finite-Rate-Catalytic (FRC) boundary condition into the US3D code. This is a high-fidelity gas-surface interaction model and the goal is to determine the model parameters and validate the US3D solutions with high quality data from VKI experiments.

Gas-surface interactions are difficult to study in shock tunnels. Although the flow is characteristic of flight conditions, the test time is on the order of microseconds and material surfaces do not have time to heat up as they would during flight. In the VKI Inductively Coupled Plasma (ICP) facility, the flow is subsonic and as a result the test times are such that the material reaches temperatures expected in flight, and high-temperature gas-surface interactions (catalysis and ablation) can be carefully observed over long test times. If the boundary layer conditions in the subsonic ICP flow can be matched to the boundary layer conditions in hypersonic flow at flight conditions, then the expected behavior of the TPS during flight can be inferred directly from ICP experiments. Specifically, VKI employs the Local Heat Transfer Simulation (LHTS) concept to match boundary layer edge properties in an ICP experiment to the corresponding hypersonic flight conditions.

There are two main goals to this Minnesota-VKI collaborative project:

- To use the US3D code to validate the LHTS approach employed by VKI. Since LHTS is a very useful and widely used technique used to interpret ICP data, a better understanding of its accuracy and potential limitations would be a valuable contribution.
- To use the US3D code to directly interpret ICP data and thereby develop new high-fidelity models for high-temperature gas-surface interactions. Basically, in the same way that US3D has been rigorously validated with shock-tunnel data (for developing gas-phase models), we plan to do the same with ICP data for gas-surface interaction models. If possible, such general models could then be applied using US3D to a large number of hypersonic problems.

As a reference, an example flow field solution obtained from the US3D code (nonequilibrium), overlaid with a local thermodynamic equilibrium (LTE) solution from VKI for the case of a plasma jet flowing over a probe-geometry is shown below in Fig.1.

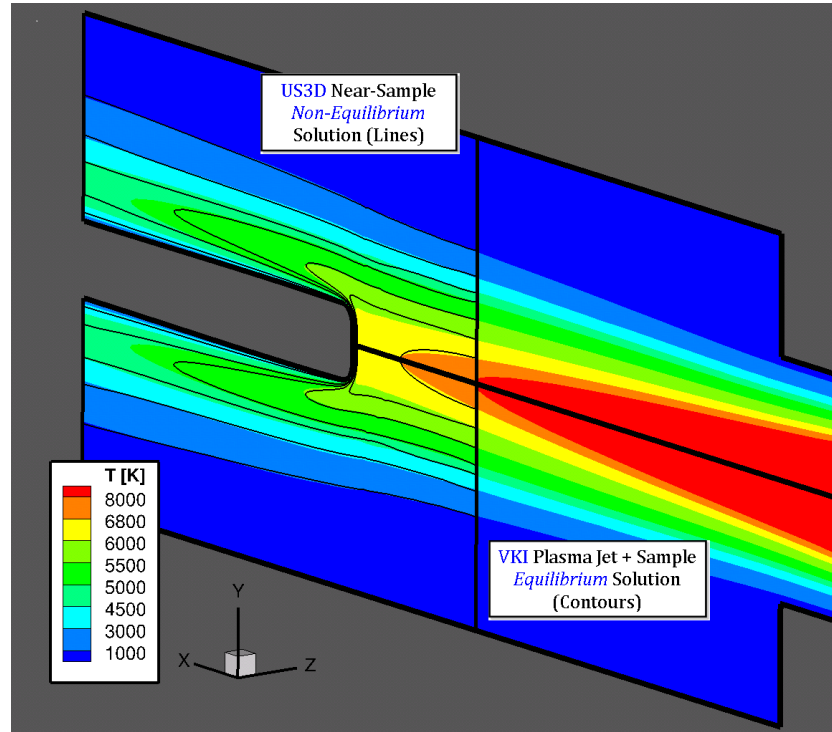


Figure 1: Representative comparison between nonequilibrium (US3D) and equilibrium (VKI-LTE) solutions for an ICP flow field.

## 2 Project Accomplishments

The ICP flow is subsonic and thus the plasma jet is expected to be very close to thermal and chemical equilibrium. The important non-equilibrium physics thus only occur within the boundary layer. Thus in all simulations, the focus is on the boundary layer profiles and the boundary layer edge conditions. Indeed the LHTS technique is used to determine the boundary layer edge conditions from an ICP experiment, after which hypersonic flight conditions are determined that result in precisely the same boundary layer edge properties. Specifically, the boundary layer edge conditions along the stagnation streamline are defined by several key parameters; namely, total enthalpy ( $H$ ), temperature ( $T$ ), bulk flow velocity ( $u$ ), and the velocity gradient,  $\frac{du}{dy}$ , where  $y$  is the radial velocity. In fact, the LHTS defines the boundary layer edge as the point of inflection in the profile (seen in upcoming figures). Thus, the simulation results presented in this section generally focus on profiles of these four variables along the stagnation line approaching the test article.

The US3D code has not been validated or tested for subsonic flow simulations prior to this research. The numerical methods used by US3D are in fact optimized specifically for hypersonic flow and thus much of the research discussed in this report is preliminary work

aimed at methodically validating US3D for subsonic plasma flows.

## 2.1 Grid convergence and US3D numerics for simple subsonic flows

A grid convergence study was performed. A typical grid density commonly employed for VKI LTE solutions is shown in Fig.2 below. US3D simulations were performed using this grid and two refined grids at twice and four times the resolution. The resulting profiles of  $u$ ,  $T$ ,  $H$ , and  $dw/dr$  are plotted in Fig.2. There is a noticeable difference in stagnation line profiles between the baseline grid and the two refined grids. As a result, it is recommended to increase the grid resolution by roughly a factor of two for future ICP simulations.

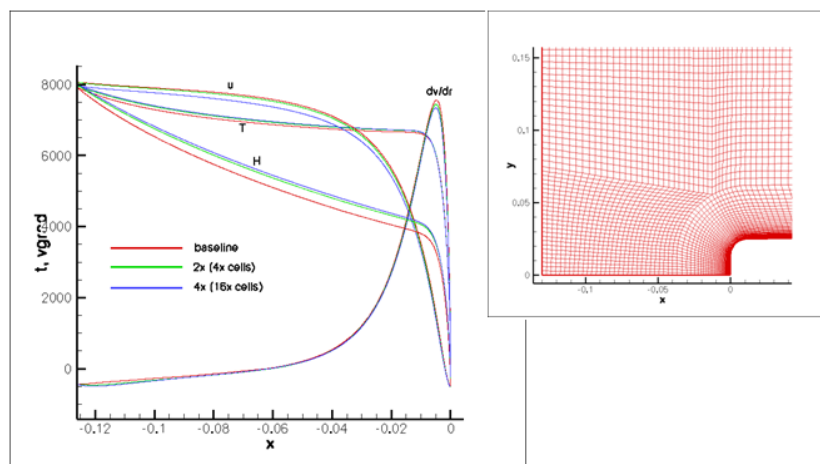


Figure 2: Grid convergence study on stagnation line profiles (left).  
Baseline mesh density (right).

Furthermore, a series of US3D simulations were performed to assess general convergence behavior, influence of domain size, and influence of the numerical stencil order-of-accuracy, on simple subsonic flow solutions. As seen in Fig.3, a uniform high-temperature air flow (typical of ICP conditions:  $T=5840$  K,  $u=209$  m/s,  $p=2000$  Pa, and  $T_{wall}=300$  K) was simulated over 10cm diameter sphere. It was determined that given uniform far-field subsonic conditions, that the US3D code was able to rapidly converged to a solution with no modifications at all. The solution was independent of the domain size (domains of 10, 20, and 40 sphere diameters were tested). Finally, it was found that various US3D stencils resulted in essentially the same solution. For example, a 6th-order accurate stencil did not noticeably change the solution compared to more standard 2nd-order accurate stencils. This is because the higher-order stencils available in US3D are designed for supersonic turbulent flows where steep gradients permeate the flow. However, this subsonic plasma jet flow is very smooth in comparison and so we conclude that the use of a 2nd order stencil is accurate. Finally, it is interesting to note that for the simulations depicted in Fig.3, there was unsteady behavior in the wake of the sphere. Although this was simulated only approximately by US3D, the wake had no noticeable effect on the stagnation line profiles (the forebody flow).



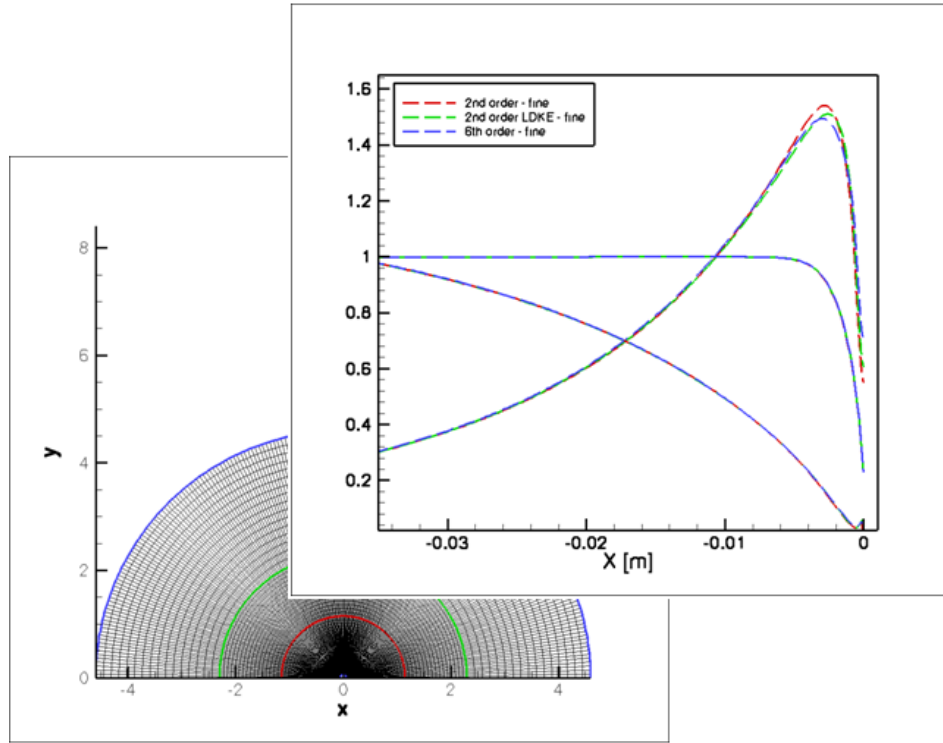


Figure 3: US3D numerics study for simple subsonic flow over a sphere.

## Conclusions:

- The baseline VKI mesh is too coarse, we recommend using 2x the resolution ( 4x the number of cells for 2D/Axi simulations).
- The unsteady wake behind a sphere (only approximately modeled by US3D), was shown to have no influence on the stagnation line profile. This supports the use of steady-state solutions for these flow problems.
- It was determined that the grid resolution in the boundary layer is very important for solution accuracy, however, using 6th order interpolation schemes provides no additional benefit over standard 2nd order methods for this type of flow.

## 2.2 Comparison of 2D vs. 3D simulations

The VKI-LTE simulations are axis-symmetric simulations. However, some experimental sample geometries of interest are not axis-symmetric. For example, a flat plate geometry with a blunted leading edge has been tested in the VKI ICP facility to study off-stagnation heating and surface catalysis. This flow is actually three-dimensional, however, VKI currently assumes that a 2D flow solution is accurate. Since the US3D code is a highly-scalable 3D code, we ran both 2D and 3D simulations with US3D and compared the boundary layer results. The 3D simulation required over 3 million elements and the solution was obtained using 256 core CPUs (solution

seen in Fig.4 below). The stagnation line profiles were found to be virtually identical between 2D and 3D solutions, as was the solution on the plane of symmetry.

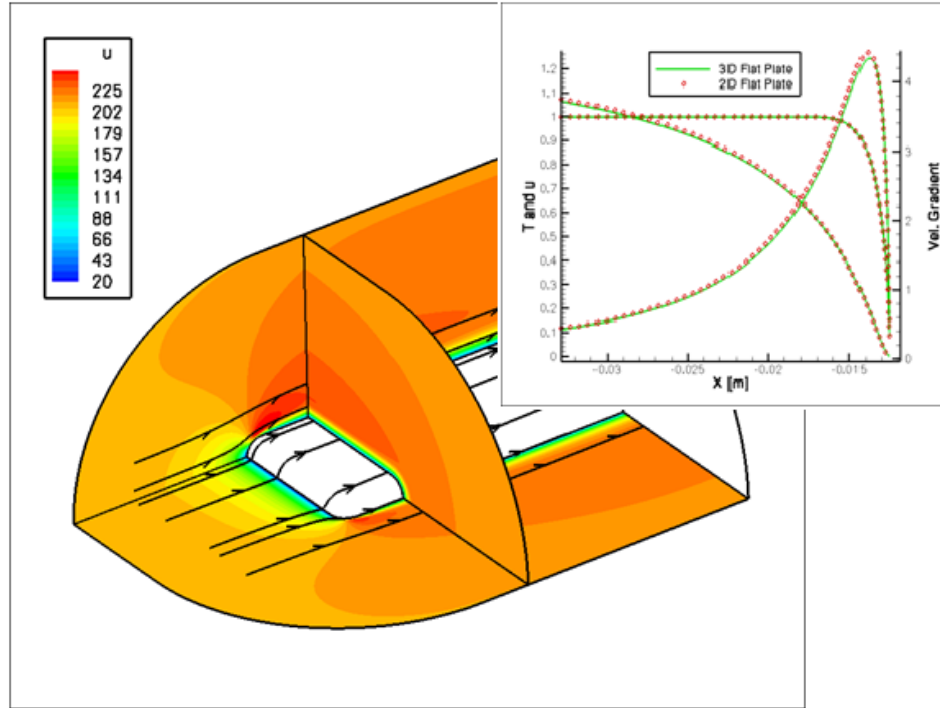


Figure 4: Stagnation line profiles ( $u$ ,  $T$  and  $dv/dx$ ) compared for 2D and 3D simulations.

## Conclusions:

- The boundary layer profiles along the stagnation line and the symmetry-plane solutions are virtually identical between 2D and 3D simulations, supporting the use of the 2D simulations used by VKI.
- However, these US3D simulations did not include a round plasma jet impinging on the 3D plate geometry. This would add another aspect to the 3D flow and these simulations should be repeated with a more realistic plasma jet to be sure the 2D simulations are still accurate.

## 2.3 Subsonic Outflow and Plasma Jet Inflow Boundary Conditions

To accurately model the ICP flow field, a realistic plasma jet profile must be specified as the inflow boundary conditions to a US3D simulation. Likewise, proper subsonic boundary conditions must be specified within US3D in order to accurately model the ICP flow.

A new subsonic outflow boundary condition was implemented and tested in the US3D code. The boundary condition extrapolates two characteristic variables from the interior solution to each outflow cell face. These two characteristics together with a prescribed background pressure are then sufficient to determine the complete gas state and these state values are

imposed in ghost-cells bordering the outflow cell faces.

Next, the US3D code was modified to specify an arbitrary plasma jet profile as an inflow boundary condition. The LTE code developed at VKI is capable of modeling the joule-heating inside the inductively coupled plasma torch; basically the process that generates the plasma. This code has been developed over a number of years and validated with data from the VKI ICP facility. It is not necessary or desirable for US3D to have this joule-heating modeling capability. Since the resulting plasma exits through a jet at equilibrium conditions, this is a more relevant inflow condition to prescribe as a US3D boundary condition. At some position in the jet flow (outside of the torch), the plasma jet profiles are extracted from the VKI LTE solution. It is noted that in the future it may be possible to experimentally measure the plasma jet properties and directly use these as inflow conditions. This simulation setup was portrayed earlier in Fig.1.

Subroutines were written to extract the plasma properties at any x-location in the jet from a VKI LTE solution and automatically prescribe these as inflow conditions within a US3D simulation. Since the VKI LTE code and US3D code do not necessarily employ the same equilibrium constants in their chemistry models, tests were performed to ensure that the equilibrium profiles predicted by LTE were the same as predicted by US3D.

An example solution corresponding to an 11 species air model is shown below in Fig. 5. Here the solid lines are the mass fractions extracted from the VKI LTE solution at a specific x-location. Therefore, these solid lines represent the inflow boundary conditions for the US3D simulation. The symbols show the final converged US3D solution for all mass fractions at the same x-location. Since the mass fractions remain virtually unchanged, this demonstrates that the initial conditions extracted from the VKI LTE solution are consistent with the equilibrium predictions of the US3D code. The progression from pure O and N in the jet core (small y) to pure O<sub>2</sub> and N<sub>2</sub> in the ambient air far from the jet (large y) is evident from Fig.5.

#### Conclusions:

- A new characteristic subsonic boundary condition was implemented in the US3D code.
- A new plasma jet profile inflow boundary condition was implemented in the US3D code. Equilibrium chemistry profiles were verified to be in agreement with VKI LTE solutions.

## 2.4 VKI LTE vs US3D solution comparisons

The main aspect of comparing VKI LTE solutions to US3D solutions is that US3D is a nonequilibrium code that does not employ a local thermodynamic equilibrium (LTE) assumption and also simulates the flow through the boundary layer edge to the surface of the object, and therefore does not couple to a boundary layer code at the boundary layer edge. Such a comparison could aid in the validation of the LHTS technique employed by VKI researchers and also ultimately validate a single consistent model (US3D) for the entire flow field that can be used to interpret the experimental data.

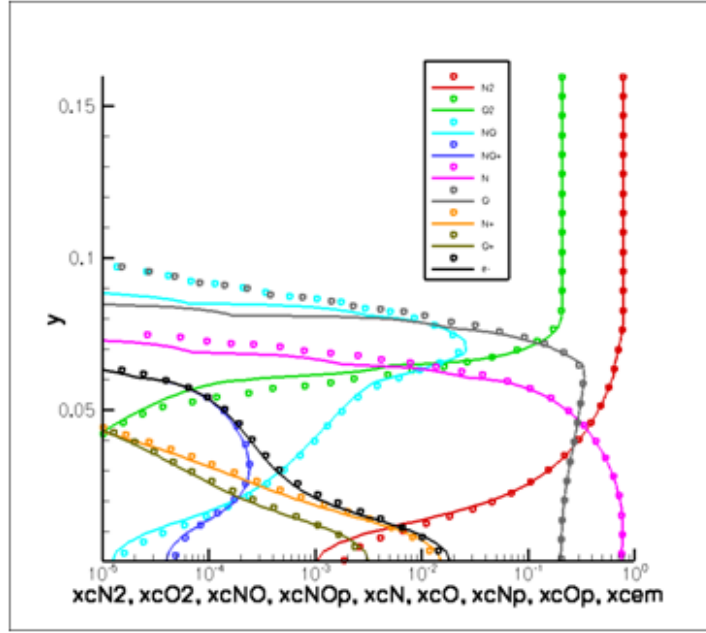


Figure 5: Mass fraction for 11-species air. Lines are extracted from VKI LTE solution (US3D inflow conditions). Symbols are final converged US3D solution.

General contour comparisons are shown below in Fig.6 for temperature and bulk velocity. The VKI LTE solution (blue lines) extends through the entire domain (torch, jet, and test object), whereas the US3D solution is initialized in the jet. In general, good agreement is found for contours of  $T$  and  $u$  in the jet and it is expected to see differences near the body since one solution is an LTE solution and the US3D solution is nonequilibrium.

One interesting test case that was investigated was performing US3D simulations of the same flow with different inflow boundary locations. As seen in Fig.7, plasma conditions were extracted from the VKI LTE code at two  $x$ -locations, and used as boundary conditions for two US3D simulations. The agreement between the two US3D results strongly supports the assumption that the plasma jet flow is indeed in thermal and chemical equilibrium. Specifically, the contours between Cut1 and Cut2 in Fig.7 are from a nonequilibrium US3D solution, yet as the flow reaches the location of Cut2, the solution still agrees with the LTE boundary conditions extracted along Cut2 from the VKI LTE code. Furthermore, both US3D solutions continue to agree downstream. This result demonstrates that according to US3D, the flow is in equilibrium, otherwise the two US3D solutions would have started to deviate and this deviation would propagate downstream. Finally, the stagnation line profiles are shown in Fig.8 for both US3D solutions and they are found to agree almost exactly.

One possible source of discrepancy comes from the top boundary condition. In reality, the plasma jet exits into a large chamber of stagnant air which would drive a large recirculating flow region to develop between the jet and the chamber walls. To include these regions in an unsteady CFD solution would be very difficult in terms of CPU time and unsteady CFD modeling. Thus the top boundary condition is set somewhat arbitrarily and a small study was completed to investigate this issue. Specifically, converged solutions were obtained when a bulk flow velocity of  $u=10, 20$ , and  $80\text{m/s}$  was imposed along the top boundary. Although it is

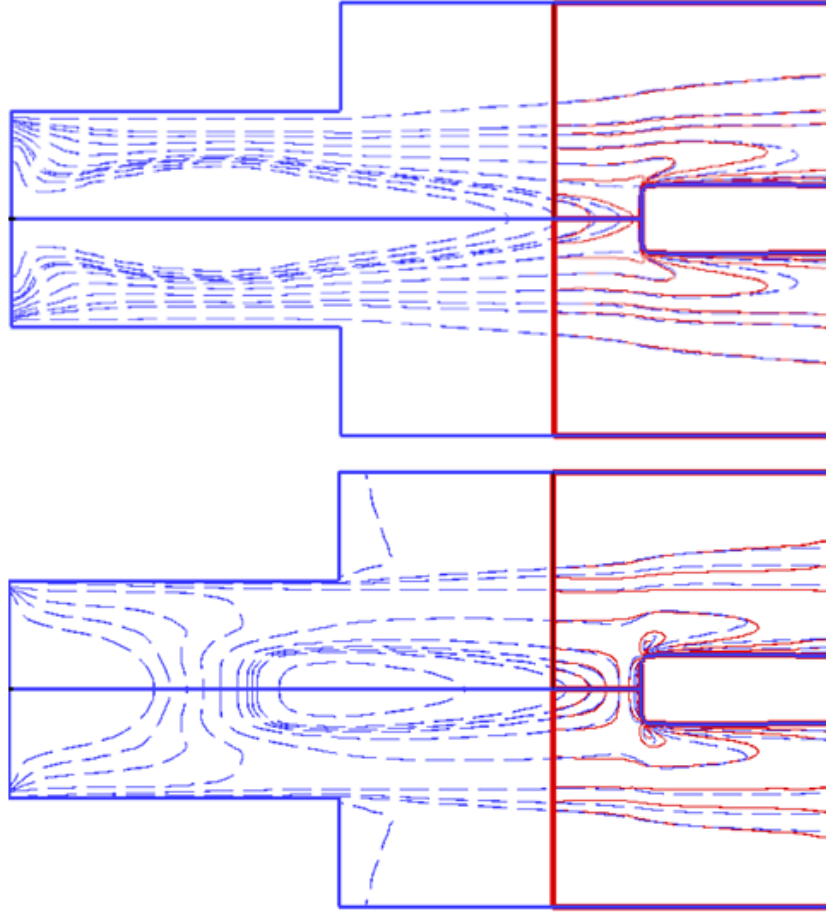


Figure 6: (top) Temperature field contours (blue-VKI LTE, red-US3D).  
(bottom) Velocity field contours (blue-VKI LTE, red-US3D).

unclear precisely what the flow properties would be along this top boundary, it is clear that this would be a region of low momentum, low temperature flow, compared to the high momentum, high temperature jet flow, and thus may not influence the solution. Indeed, we found that the velocity imposed along the top boundary has little to no influence on the stagnation line flow properties (or flow near the test object) as long as the imposed velocity is low ( $u \leq 80 \text{ m/s}$ ). The higher the velocity set at the top boundary, the faster the convergence of the solution, so typically a velocity of  $u=20 \text{ m/s}$  was used for the remaining simulations. Figure 9(left) shows the 3 jet profiles resulting from these three velocity boundary conditions 1cm upstream of the test-object. Figure 9(right), shows the stagnation line profiles of the variables of interest, where no noticeable difference is observed.

The most important comparison between US3D and VKI LTE solutions is again the boundary layer variables along the stagnation streamline. These are plotted in Fig.10. Here we see excellent agreement for bulk velocity and density, however, we see large discrepancies for temperature and total enthalpy. US3D is a nonequilibrium code, that employs a two-temperature model ( $T$  and  $T_{vib}$ ). We expected to see thermal equilibrium for this flow and therefore  $T=T_{vib}$  at virtually all points in the flow. However, we see anomalous behavior of  $T_{vib}$  along the plasma jet core, near the inflow. Furthermore, we see a 7% discrepancy in total enthalpy persist through-

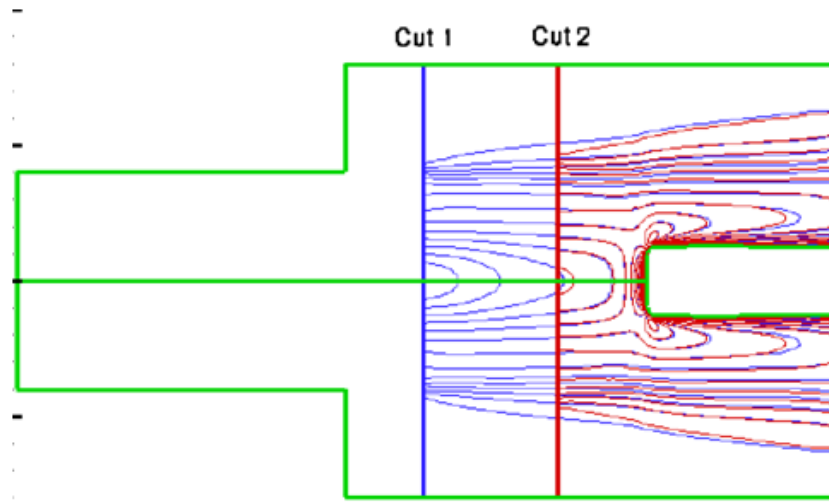


Figure 7: Two US3D solutions (velocity contours) initialized at two different locations in the plasma jet.

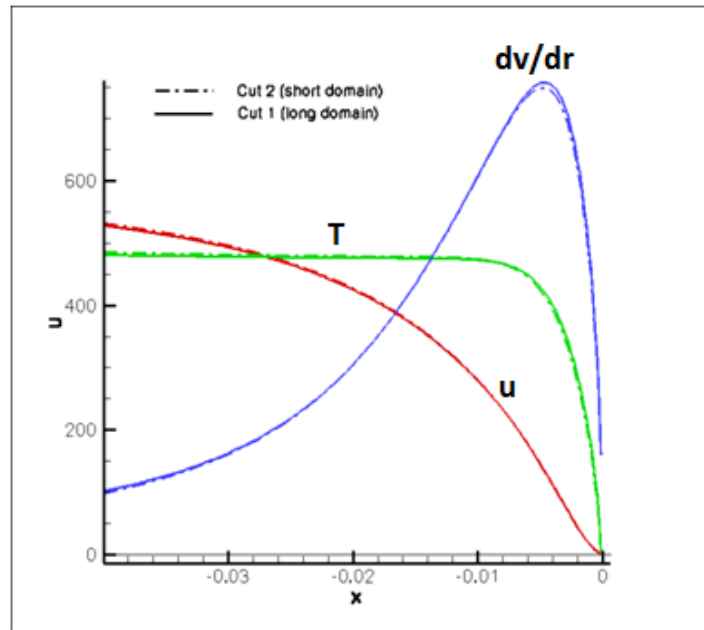


Figure 8: Stagnation line solutions for the two US3D solutions shown in Fig.7

out the flow. This enthalpy discrepancy is even evident in the first few cells near the inflow boundary condition, despite both simulations specifying the same plasma inflow conditions.

After substantial investigation, code-to-code comparisons, and modification of physical models, it was determined that all of these discrepancies are due to the fact that US3D does not currently model electronic energy. If the US3D solution is post-processed to account for electronic energy modes, the computed enthalpy at the inflow moves into near perfect agreement with the VKI LTE code as seen in Fig.11. However, this post-processing assumes LTE at each point in the US3D solution to determine the enthalpy. Since we are attempting to prove the LTE assumption is valid, it is required to add a nonequilibrium model for electronic energy to the

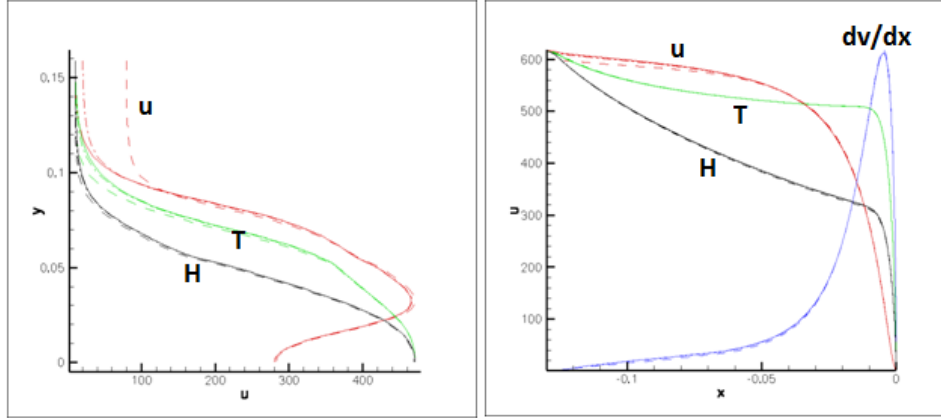


Figure 9: (left) jet profile solution 1 cm upstream of the test-object. Three profiles are shown corresponding to three top-boundary velocity values ( $u = 10, 20, 80$  m/s).  
(right) Stagnation line profiles corresponding to the three solutions.

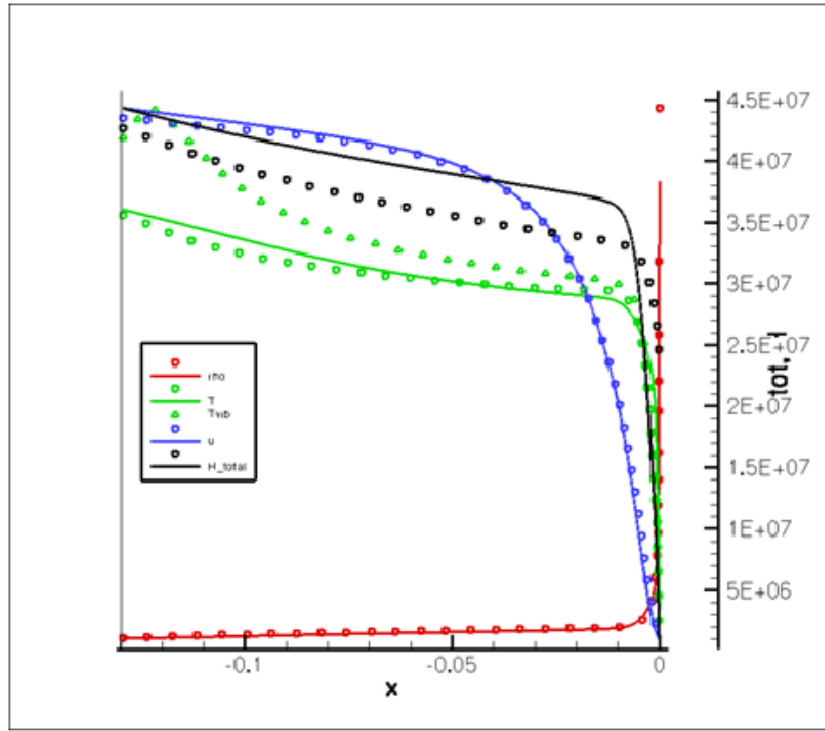


Figure 10: Stagnation line solutions from the VKI LTE code (lines) and from the US3D code (symbols).

US3D code.

Adding a model for electronic energy would also eliminate the anomalous behavior of  $T_{vib}$ . The problem is that in the plasma jet core the temperatures are so high that the air is completely dissociated (mass fractions of diatomics are close to machine zero). This situation has never been encountered by the US3D code since in hypersonic flows the gas is never completely dissociated due to nonequilibrium effects. Numerically, the vibrational temperature is computed

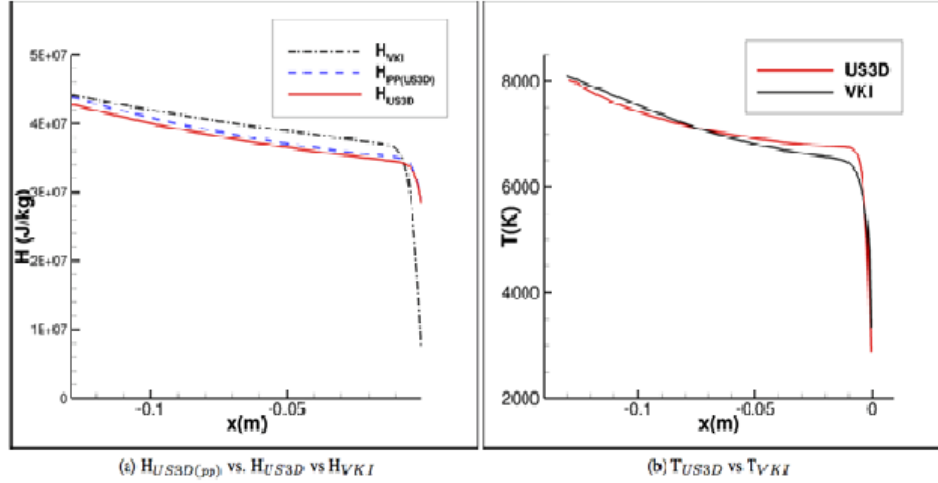


Figure 11: Stagnation line enthalpy and temperature profiles for US3D with electronic energy post-processing compared to the VKI LTE solution.

from the vibrational energy considering the diatomic species that this energy is distributed among. However, in the jet core there is essentially no vibrational energy and more troublesome, there are no diatomics present. As a result, the value of  $T_{vib}$  is not well defined and numerically its value has large error. To some degree the value of  $T_{vib}$  doesn't influence the solution since there is almost no vibrational energy present in that region anyway, however, the problem is that the dissociation/recombination model employed by US3D is Parks T- $T_v$  model. So  $T_{vib}$  is specifically used to set the dissociation and recombination rates. Thus even if the anomalous  $T_{vib}$  value does not influence the vibrational energy equation, it strongly influences the chemistry. As a result, it is important to modify US3D to avoid such numerical problems. By adding electronic energy and coupling this to the vibrational temperature this would mean that even with no diatomics there will be electronically excited atoms present. This electronic energy would then result in a well-defined value for the combined vibrational-electronic temperature.

#### Conclusions:

- Good agreement between US3D and VKI LTE solutions was found for hydrodynamic properties of the plasma jet and boundary layer. However, significant discrepancies were found in the translational and vibrational temperatures and total enthalpy throughout the simulation domain, including near the inflow boundary.
- It was determined that these discrepancies are due to the fact that US3D does not currently model electronic energy.
- It was determined that implementing electronic energy and coupling with vibrational energy (a combined electronic-vibration temperature) will bring the enthalpies into agreement and also eliminate numerical issues regarding the vibrational temperature.



### 3 Future Work

This collaborative project that involved a small amount of initial funding to have Prof. Schwartzentruber visit and work at VKI for 3 months is the start of a much longer term and productive collaboration between the University of Minnesota (computational expertise) and VKI (experimental expertise). This research is directly related to a large Multi-University-Research -Initiative (MURI) funded by AFOSR and based at the University of Minnesota on Fundamental Processes in Hypersonic Flows. Collaborative work will continue on this specific project over the next year.

Specifically, we are in the process of adding a model for electronic energy to the US3D code. We are also implementing/testing a variety of gas-surface interaction boundary conditions. Within the next few months we expect to have full US3D solutions of the ICP flows with all required physical models for both gas-phase and gas-surface reactions. At this point, direct comparison with ICP experimental results will be performed. We expect two publications towards the end of 2012. The first involving validation of the LHTS technique by full nonequilibrium US3D simulation and the second involving interpretation of experimental measurements (stagnation and off-stagnation data) for the creation of new gas-surface interaction models.

## Part II

# Numerical simulation of plasma jet and gas-surface interaction around blunted plate with COOLFluid

## Introduction

This document presents the computational model (physico-chemical model and numerical method) and some preliminary results for the numerical analysis of a Thermal Protection System (TPS) test in the VKI Plasmatron wind tunnel. The experiment consists of a high-enthalpy plasma jet impinging on a flat plate with blunted leading edge, featuring different Thermal Protection System materials with different catalytic properties. The numerical simulation has been performed with the aerothermodynamic code inside the COOLFluid platform. Both nonequilibrium and gas-surface interaction effects have been taken into account in our investigation.

### 0.1 COOLFluid platform

COOLFluid (**C**omputational **O**bject **O**riented **L**ibraries for **F**luid **D**ynamics) [1, 2, 3, 4] is VKI collaborative software environment for high-performance scientific computing where different numerical techniques, physical models, post-processing algorithms can coexist and work together. Herein, each numerical method or physical model is encapsulated into an independent dynamic module (or *plug-in* library) that can be loaded on demand by user-defined applications. Some of the main features of COOLFluid include:

- different multidimensional parallel solvers for compressible and incompressible flows, based on different space discretization techniques for unstructured meshes, including cell-centered Finite Volume (FV), Residual Distribution Schemes (RDS), Spectral Finite Volume/Difference and standard Finite Element (FE).
- explicit (Runge Kutta n-order) and implicit (3 point-backward, Crank-Nicholson, time-limited) time marching schemes;
- interfaces to several linear system solver packages such as PETSc, Trilinos, Pardiso, etc.
- compressible Reynolds averaged Navier-Stokes with  $k-\omega$ , BSL, SST and Spalart-Almaras turbulence models;
- multi-temperature and Collisional Radiative models for arbitrary gas mixtures in thermo-chemical nonequilibrium;
- Magneto-Hydrodynamics models for Space Weather applications;
- coupling algorithms for multi-physics and multi-domain simulations, allowing both strong and loose coupling
- robust mesh deformation algorithms.

**Distribution A: Approved for public release; distribution is unlimited.**

# 1 Physical modeling

The sets of governing PDE's (Navier-Stokes) describing a 2D axisymmetric flow in a continuum regime can be expressed in conservative and hypervectorial form as:

$$\frac{\partial \mathbf{U}}{\partial \mathbf{P}} \frac{\partial r \mathbf{P}}{\partial t} + \frac{\partial r \mathbf{F}_x^c}{\partial x} + \frac{\partial r \mathbf{F}_r^c}{\partial r} = \frac{\partial r \mathbf{F}_x^d}{\partial x} + \frac{\partial r \mathbf{F}_r^d}{\partial r} + \mathbf{S} \quad (1)$$

where  $x$  and  $r$  are the axial and radial directions. Herein, according to the terminology adopted in COOLFluid,  $\mathbf{U}$  are the conservative variables,  $\mathbf{P}$  the *update* variables,  $\mathbf{F}^c$  and  $\mathbf{F}^d$  respectively the convective and diffusive fluxes,  $\mathbf{S}$  the source term.

## 1.1 Park's 2-temperature model

In the case of a gas mixture in thermal and chemical nonequilibrium (TCNEQ), the conservative and update (or natural) variables corresponding to a 2-temperature model [5, 6] can be expressed as follows:

$$\mathbf{U} = (\rho_s, \rho \mathbf{u}, \rho E, \rho e_V)^T, \quad \mathbf{P} = (\rho_s, \mathbf{u}, T, T_V)^T \quad (2)$$

where, in particular,  $\rho_s$  represents the partial densities,  $e_V$  is the vibrational-electronic energy per unit mass and  $T_V$  stands for the vibrational-electronic temperature. In this case, the convective and diffusive fluxes are defined by:

$$\mathbf{F}^c = \begin{pmatrix} \rho_s \mathbf{u} \\ \rho \mathbf{u} \mathbf{u} + p \hat{I} \\ \rho \mathbf{u} H \\ \rho \mathbf{u} e^V \end{pmatrix}, \quad \mathbf{F}^d = \begin{pmatrix} -\rho_s \mathbf{u}_s^d \\ \bar{\bar{\tau}} \\ (\bar{\bar{\tau}} \cdot \mathbf{u})^T - \mathbf{q} \\ -\mathbf{q}_V \end{pmatrix}. \quad (3)$$

where the pressure  $p$  is given by the following equation of state:

$$p = p_e + \sum_{s \neq e} p_s = \rho R \left( T_e \frac{y_e}{M_e} + T \sum_{s \neq e} \frac{y_s}{M_s} \right) \quad (4)$$

where, in particular,  $p_e$  represents the electron pressure,  $y_s$  are the species mass fractions,  $M_s$  the species molar masses and  $T_e = T_V$  if thermal nonequilibrium is assumed.

The tensor of viscous stresses  $\bar{\bar{\tau}}$  appearing in Eq. 3 is defined as

$$\tau_{ij} = \mu \left[ \left( \frac{\partial u_j}{\partial x_i} + \frac{\partial u_i}{\partial x_j} \right) - \frac{2}{3} \nabla \cdot \mathbf{u} \delta_{ij} \right] - \delta_{ij} \frac{2}{3} \mu \frac{v}{r} \quad (5)$$

and it is computed using Stokes' hypothesis of negligible bulk viscosity effects. Herein, the dynamic viscosity  $\mu$  is computed rigorously from kinetic theory by using the transport algorithms described in [7, 8].

The mass diffusion fluxes  $\rho_s \mathbf{u}_s^d$  are computed by solving the Stefan-Maxwell system [9, 10] of equations which consist of a linear system (in the diffusion fluxes) of as many equations as the chemical species are present in the mixture. This system is supplemented by the auxiliary

condition that the sum of the diffusion fluxes is zero. Moreover, by imposing the ambipolar constraint stating that

$$n_e = n_i = \sum_{s=\text{ions}} n_s \quad (6)$$

where  $n_e$  is the electron number density and  $n_i$  is the ionic number density, the flow field in an ionized gas mixture can be considered electrically neutral [9, 11].

The roto-translational and vibrational-electronic heat fluxes  $\mathbf{q}$  and  $\mathbf{q}_V$  are defined as

$$\mathbf{q} = -\lambda \nabla T - \lambda_V \nabla T_V - \sum_s \rho_s \mathbf{u}_s h_s \quad (7)$$

$$\mathbf{q}_V = -\lambda_V \nabla T_V - \sum_s \rho_s \mathbf{u}_s h_s^v \quad (8)$$

where the  $\lambda$  is the roto-translational thermal conductivity,  $\lambda_V$  is the vibrational-electronic thermal conductivity and the species enthalpies  $h_s$  are given by

$$h_s = h_t^s(T) + h_e^s(T_V) + h_f^s \quad \text{atoms} \quad (9)$$

$$h_s = h_t^s(T) + h_r^s(T) + h_v^s(T_V) + h_e^s(T_V) + h_f^s \quad \text{molecules} \quad (10)$$

$$h_s = h_t^s(T_V) \quad \text{free electrons} \quad (11)$$

where  $h_t^s, h_r^s, h_v^s, h_e^s, h_f^s$  are respectively the translational, rotational, vibrational, electronic and formation enthalpies for species  $s$ .

### 1.1.1 Mass production / destruction terms

The source terms in Eq. 2 can be expressed as

$$\mathbf{S} = \begin{pmatrix} 0 \\ 0 \\ p - \tau_{\theta\theta} \\ 0 \\ 0 \end{pmatrix} + \frac{1}{r} \begin{pmatrix} \dot{\omega}_s \\ 0 \\ 0 \\ 0 \\ -p_e \nabla \mathbf{u} + \Omega^{vt} + \Omega^{et} + \Omega^{CV} - \Omega^I \end{pmatrix} \quad (12)$$

In the first contribution, due the axisymmetric formulation, an additional viscous stress component  $\tau_{\theta\theta}$  in the circumferential direction  $\theta$  reads:

$$\tau_{\theta\theta} = -\frac{2}{3}\mu \left( \frac{\partial u}{\partial x} + \frac{\partial v}{\partial r} - 2\frac{v}{r} \right) \quad (13)$$

The mass production/destruction term  $\dot{\omega}_s$  for chemical species with partial densities  $\rho_s$  which appears in Eq. 12 is formulated as follows:

$$\frac{\dot{\omega}_s}{M_s} = \sum_{r=1}^{Nr} (\nu_{sr}'' - \nu_{sr}') \left\{ k_{fr} \prod_{j=1}^{Ns} \left( \frac{\rho_j}{M_j} \right)^{\nu_{jr}'} - k_{br} \prod_{j=1}^{Ns} \left( \frac{\rho_j}{M_j} \right)^{\nu_{jr}''} \right\} \quad (14)$$

where the forward reaction rates  $k_{fr}$  corresponding to a 5-species neutral air mixture used in this work are taken from [12].

### 1.1.2 Energy exchange terms

$\Omega^{vt}$ , the energy exchange (relaxation) between vibrational and translational modes due to collisions can be expressed as

$$\Omega^{vt} = \sum_m \rho_m \frac{e_m^{v,*} - e_m^v}{\tau_m}, \quad (15)$$

where  $e_m^{v,*}$  is the equilibrium vibrational energies of molecules  $m$  evaluated at the roto-translational temperature, according to the Landau-Teller formulation [13]. The latter assumes mono-quantum energy transfers: in the collision between two molecules or between a molecule and an electron, one colliding particle can gain or lose only one energetic level, while the energy of the other particle remains unchanged. The relaxation time  $\tau_m$  is given by Millikan and White [14] with Park's correction for high temperatures [15]:

$$\tau_m = \tau_m^{MW}(p, T) + \overbrace{(\sigma_m c_m n_m)^{-1}}^{\tau_{\text{Park}}} \quad (16)$$

where  $\sigma_m$  is the effective cross section for vibrational relaxation processes,  $c_m$  is the average molecular velocity of molecule  $m$  and  $n_m$  is the number density.

Finally,  $\Omega^{CV}$  stands for the vibrational energy lost or gained due to molecular dissociation or recombination:

$$\Omega^{CV} = \sum_m \dot{\omega}_m \hat{D}_m \quad (17)$$

Among the several possibilities for the choice of  $\hat{D}_m$  reported in literature, the simplest one is to impose  $\hat{D}_m = e_m^v$ , with  $e_m^v$  being the vibrational energy of the molecule.  $\Omega^{et}$  represents the energy exchange due to inelastic collisions between the electrons and the heavy particles:

$$\Omega^{et} = 2\rho_e \frac{3}{2} R(T - T^e) \sum_{s \neq e} \frac{\nu_{e,s}}{M_s} \quad (18)$$

where  $\nu_{e,s}$  is the effective collision frequency of electron with heavy particles as defined in [5].  $\Omega^I$  corresponds to the energy loss due to electron impact ionization and is given by

$$\Omega^I = \sum_{\text{ions}} \dot{n}_{e,s} \hat{I}_s \quad (19)$$

where  $\dot{n}_{e,s}$  is the molar rate of production of species  $s$  and  $\hat{I}_s$  is the energy lost per unit mole by a free electron in producing species  $s$  by electron impact ionization [11].

For a broader introduction to the thermodynamic, chemical and transport properties modeling employed in this work, the reader may refer to [5, 4, 7, 8, 16, 6, 17].

## 1.2 Modeling of ICP facility

Inductively Coupled Plasma (ICP) wind tunnels are usually hard to simulate due to the complexity of the problem. The gas is injected into the wind tunnel and then heated by means of an external inductor, then the flow reaches very high temperatures in the torch ( $\sim 10000K$ ). That implies that there are several subsystems interacting in this kind of problems: on one hand, the flow field, governed by the Navier-Stokes equations at Local Thermodynamic Equilibrium (LTE) (1); on the other hand, the electromagnetic field created by the inductor. Both subsystems are coupled and have to be solved simultaneously.

### 1.2.1 Electromagnetic field equations

The electromagnetic field equations are quickly presented in this section. The equation of the electric field induced by the torch reads:

$$\frac{\partial^2 E}{\partial x^2} + \frac{1}{r} \frac{\partial}{\partial r} \left( r \frac{\partial E}{\partial r} \right) - \frac{E}{r^2} - i\omega\mu_0\sigma E = -i\omega\mu_0\sigma I_c \sum_{i=1}^{n_{coils}} \delta(\vec{r} - \vec{r}_i) \quad (20)$$

Where the electric field  $E$  is a complex variable. We can take into account that the total field is equal to the sum of the electric field induced by the coils  $E_v$  and the electric field produced by the currents running into the plasma  $E_p$ :

$$E = E_v + E_p$$

Thus, Equation (20) can be separated into two different equations:

$$\frac{1}{r} \frac{\partial}{\partial r} \left( r \frac{\partial E_v}{\partial r} \right) + \frac{\partial^2 E_v}{\partial x^2} - \frac{E_v}{r^2} = -i\omega\mu_0 I_c \sum_{i=1}^{n_{coils}} \delta(\vec{r} - \vec{r}_i) \quad (21)$$

$$\frac{1}{r} \frac{\partial}{\partial r} \left( r \frac{\partial E_p}{\partial r} \right) + \frac{\partial^2 E_p}{\partial x^2} - \frac{E_p}{r^2} = i\omega\mu_0\sigma (E_v + E_p) \quad (22)$$

Equation (21) can be solved analytically, whereas the solution of equation (22) is more difficult to be obtained, and one needs an electromagnetic field model to compute  $E_p$ .

### 1.2.2 Coupled system

The Navier-Stokes equations and the electromagnetic field equations are coupled and solved together. The torch creates an electric field that interacts with the ionized plasma, affecting its movement by means of the Lorentz force. Besides, the electromagnetic field produces also changes in the flow, increasing its temperature because of the Joule effect. On the other hand, the temperature changes influence the electric conductivity of the air, meaning that, in equation (20), the induced electric field will be also affected by the temperature changes. To sum up, these two systems of equations are coupled in both directions: the solution of the electric field system affects the Navier-Stokes system and *vice versa*.

A detailed explanation about the computation and the implementation of the Lorentz force and the Joule effect can be found in [18] and is detailed below.

**Lorentz force.** The motion of a particle is governed by the Lorentz force, which acts on a point charge due to the electromagnetic field. It is given by the following equation:

$$\frac{\partial m\vec{v}}{\partial t} = \vec{F}_L = q(\vec{E} + \vec{v} \times \vec{B}) \quad (23)$$

where  $\vec{F}_L$  is the force (in newtons),  $\vec{E}$  and  $\vec{B}$  are the electric (in volts per meter) and magnetic field (in Tesla's),  $q$  is the electric charge of the particle (in coulombs) and  $\vec{v}$  is the instantaneous

velocity of the particle (in meters per second),  $m\vec{v}$  the momentum of the particle. Combining the following expression:

$$\vec{E}' = \vec{E} + \vec{u} \times \vec{B} \quad (24)$$

of the electric field in a frame of reference moving with the mean velocity of the flow, with the definition of  $V_i$ , we can write the Lorentz force applied to a particle  $i$  as follows:

$$\vec{F}_{L,i} = q_i(\vec{E} + \vec{v} \times \vec{B}) = q_i(\vec{E} + (\vec{u} + \vec{V}_i) \times \vec{B}) = q_i(\vec{E} + \vec{u} \times \vec{B} + \vec{V}_i \times \vec{B}) = q_i(\vec{E} + \vec{v}_i \times \vec{B}) \quad (25)$$

**Joule Heating.** The heat source term due to Joule effect, also known as ohmic heating, applies to any conductor when electric current is passing through it. It is defined by the following equation:

$$P_J = \sum_i \vec{n}_i q_i < \vec{V}_i \times \vec{B} = \vec{J}_c \cdot \vec{E}_I, \quad (26)$$

where  $i$  is a charged particle,  $\sum_i n_i q_i < \vec{F}_i \cdot \vec{V}_i >$  is the power developed by a force on a particle  $\vec{F}_i$ , and  $\vec{J}_c$  is the conduction current density. This equation further simplifies to

$$P_J = \sigma \vec{E}_I \cdot \vec{E}_I \quad (27)$$

The neutral plasma hypothesis  $\sum_i n_i q_i = 0$ , the Reynolds magnetic number and the ambipolar diffusion hypothesis has been used to derive these expressions. The root mean square of  $\vec{P}_J$  will be used as source term in the N-S system, and it can be easily derived

$$< P_J > = < \vec{E}_I \cdot \vec{E}_I > = \sigma < E_\theta \cdot E_\theta > = \sigma < E_{\theta,c}^2 (e^{i\omega t})^2 2 > = \frac{1}{2} \sigma E_{\theta,c}^2 \quad (28)$$

The implemented equation uses the real and imaginary part, as follows:

$$< P_J > = \frac{1}{2} \sigma (E_{Re}^2 + E_{\theta,c Im}^2) \quad (29)$$

## 2 Numerical method

### 2.1 Space discretization

All the results to be presented have been obtained by means of a parallel FV solver for unstructured grids implemented within COOLFluidD. The FV discretization is applied to the system of governing equations written in integral conservation form:

$$\frac{\partial}{\partial t} \int_{\Omega} \mathbf{U} \, d\Omega + \oint_{\partial\Omega} \mathbf{F}^c \cdot \mathbf{n} \, d\partial\Omega = \oint_{\partial\Omega} \mathbf{F}^d \cdot \mathbf{n} \, d\partial\Omega = \int_{\Omega} \mathbf{S} \, d\Omega \quad (30)$$

where  $\mathbf{F}^c$  and  $\mathbf{F}^d$  represent respectively the convective and diffusive fluxes, while  $\mathbf{S}$  contains the reaction terms. We apply a conventional cell centered approximation, which assumes solution vectors located at the centroid of each computational cell. Inverse-distance weighted least square reconstruction [19] is utilized to yield second order accuracy. Oscillation free solutions are obtained with the multidimensional limiter of Venkatakrishnan [20]. A modified version of the AUSM+ scheme [21, 4] has been used to discretize the convective fluxes in all our computations, as detailed hereafter.

### 2.1.1 AUSM+ scheme

The AUSM+ scheme [21] offers a good compromise between robustness and accuracy, while being not prone to the carbuncle phenomenon. The AUSM+ scheme relies on the splitting between a convective and a pressure component:

$$\mathbf{F}_{1/2}(\mathbf{U}_L, \mathbf{U}_R, \mathbf{n}) = \mathbf{F}^{(c)} + \mathbf{F}^{(p)} = \dot{m}_{1/2} \mathbf{\Psi}_{L/R} + \mathbf{p}_{1/2} \quad (31)$$

Herein, in the case of a gas mixture in thermal and chemical nonequilibrium with  $N_s$  chemical components and  $N_m$  molecules, which is the case of interest here, the scalar mass flux  $\dot{m}$ , the interface Mach number  $M_{1/2}$ , the vector quantity  $\mathbf{\Psi}$  and the pressure flux  $\mathbf{F}^{(p)}$  can be expressed respectively as:

$$\dot{m}_{1/2} = M_{1/2} a_{1/2} \begin{cases} \rho_L & \text{if } M_{1/2} > 1, \\ \rho_R & \text{otherwise} \end{cases} \quad (32)$$

$$M_{1/2} = \mathcal{M}^+(M_L) + \mathcal{M}^-(M_R) \quad (33)$$

$$\mathbf{\Psi} = [y_s, \mathbf{v}, H, y_m E_m^v] \quad (34)$$

$$\mathbf{p}_{1/2} = \mathcal{P}^+(M_L) p_L \mathbf{n} + \mathcal{P}^-(M_R) p_R \mathbf{n} \quad (35)$$

where the actual definition of the split Mach number  $\mathcal{M}^\pm$  and the split pressure functions  $\mathcal{P}^\pm$  can be found in [21]. The interface speed of sound  $a_{1/2}$  appearing in Eq. 32 is defined

$$a_{1/2} = \min(\tilde{a}_L, \tilde{a}_R), \quad \tilde{a} = \frac{a^{*2}}{\max(a^*, |q_n|)} \quad (36)$$

where for the critical speed of sound, originally defined as  $a^* = \sqrt{\frac{2(\gamma-1)}{\gamma+1}} H$  in [21], we adopt a more suitable definition [4] in our computations dealing with flows in thermo-chemical nonequilibrium:

$$a^* = \sqrt{\frac{2\tilde{\gamma}(\tilde{\gamma}-1)}{2\tilde{\gamma} + \tilde{\gamma}(\tilde{\gamma}-1)}} H \quad (37)$$

where the frozen specific heat ratio  $\tilde{\gamma} = \frac{\sum_s y_s \partial h_s / \partial T}{\sum_s y_s \partial e_s / \partial T}$  and the equivalent specific heat ratio  $\bar{\gamma} = 1 + p/\rho e$  are considered.

### 2.1.2 Discretization of diffusive Fluxes

The discretization of the diffusive term in Eq. 30 leads to:

$$\oint_{\Sigma} \mathbf{F}^d \cdot \mathbf{n} d\Sigma = \sum_{f=1}^{N_f} \mathbf{G}_f \Sigma_f \quad (38)$$

where  $\mathbf{G}_f = \mathbf{F}_f^d \cdot \mathbf{n}_f$  and the diffusive fluxes  $\mathbf{F}^d$  typically depend on the variables  $\mathbf{P}$  and their gradients, i.e.  $\mathbf{F}^d = \mathbf{F}^d(\mathbf{P}, \nabla \mathbf{P})$ .



**Gradient calculation: diamond control volume.** The application of Green-Gauss' theorem within a chosen control volume  $\Omega^v$  can be used to determine the above mentioned gradients:

$$\nabla \mathbf{P} = \frac{1}{\Omega^v} \int_{\Omega^v} \nabla \mathbf{P} d\Omega^v = \frac{1}{\Omega^v} \oint_{\Sigma^v} \mathbf{P} \mathbf{n} d\Sigma^v \quad (39)$$

A popular choice for  $\Omega^v$  on unstructured meshes is a diamond-shaped volume [22, 23] like the one in Fig. 12 which is built around the considered face and which includes all the face nodes, the left and right cell centers as vertexes.

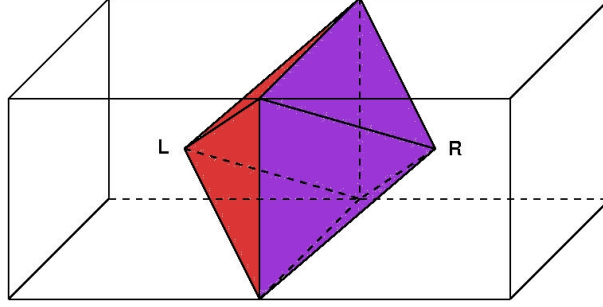


Figure 12: Diamond control volume for the calculation of the gradients for the diffusive fluxes.

The discretized version of Eq. 39 becomes:

$$\nabla \mathbf{P} = \frac{1}{\Omega^v} \sum_{f=1}^{N_f} \bar{\mathbf{P}}_f \mathbf{n}_f \Sigma_f^v, \quad \text{with} \quad \bar{\mathbf{P}}_f = \frac{1}{N_n^f} \sum_{j=1}^{N_n^f} \mathbf{P}_j^f \quad (40)$$

where  $\bar{\mathbf{P}}_f$  is a face-averaged value of  $\mathbf{P}$  calculated from the values  $\mathbf{P}_j^f$  in the vertices of the diamond volume, whose number of faces is  $N_f$ . Moreover,  $N_n^f$  is the number of vertexes in each face  $f$  of the control volume, i.e.  $N_n^f$  is equal to the space dimension of the problem (2 or 3).

**Gradient calculation: Kim's method.** Alternatively, the method extensively described in [24] can be used to compute the gradients. In this case, the cell-based solution gradients, computed via a least square reconstruction, are corrected and projected onto the faces. This method is known to provide superior accuracy and robustness on high-aspect ratio cells.

### 2.1.3 Discretization of source Terms

The discretization of the source term appearing on the left-hand-side of 30 is based on the cell centered value in a given cell  $i$ :

$$\int_{\Omega} \mathbf{S}(\mathbf{P}) d\Omega \approx \mathbf{S}(\mathbf{P}_i) \Omega_i = \mathbf{S}_i \Omega_i \quad (41)$$

When the source term includes derivatives of some dependent variable  $p$  (e.g. the stress term  $\tau_{\theta\theta}$  appearing in the case of axisymmetric Navier-Stokes), these are calculated by applying the Green-Gauss theorem, similarly to what explained in Sec. 2.1.2:

$$\nabla p = \frac{1}{\Omega_i} \int_{\Omega_i} \nabla p \, d\Omega_i = \frac{1}{\Omega_i} \oint_{\Sigma_i} p \, \mathbf{n} \, d\Sigma_i \quad (42)$$

In this case, however, the chosen control volume coincides with the volume of the current cell,  $\Omega_i$ , while a diamond-shaped one was used for the computation of the diffusive fluxes. The discretized version of Eq. 42 is identical to Eq. 40.

#### 2.1.4 Boundary conditions for nonequilibrium solver

**Radiative equilibrium wall.** The radiative equilibrium wall boundary condition consists in imposing that the heat released from the gas into the wall by conduction ( $q_g^{cond}$ ) and convection ( $q_g^{conv}$ ) is exactly balanced by the heat lost by radiation ( $q_r$ ) from the wall itself. This translates into the non linear equation:

$$Q(T_w) = q_g^{cond} + q_g^{conv} + q_r = 0 \quad (43)$$

to be solved iteratively at the wall. After having substituted the actual expressions for all terms, this expression becomes:

$$Q(T_w) = - \left( \lambda \frac{\partial T}{\partial n} + \sum_m^{N_m} \lambda_m^v \frac{\partial T_m^v}{\partial n} \right) + \sum_s^{N_s} h_s \mathbf{J}_s \cdot \mathbf{n}_w - \sigma (\epsilon_w^e T_w^4 - \epsilon_w^a T_\infty^4) = 0 \quad (44)$$

where  $\sigma = 5.67 \cdot 10^{-8} [W/m^2/K^4]$  is the Stefan-Boltzmann constant,  $\epsilon_w^e$  and  $\epsilon_w^a$  are respectively the wall emissivity and absorptivity and  $T_\infty$  is the distant body temperature. The solution  $T_w$  of the non linear equation  $Q(T_w) = 0$  is obtained by applying a Newton procedure, where in order to enhance numerical robustness the maximum variation of wall temperature for each boundary face between two subsequent time steps is limited to a user-defined value (typically 100-200 K).

**Super catalytic wall with LTE.** This condition imposes the chemical composition of the gas mixture at the wall to be equal to the equilibrium values. Under the local thermodynamic and chemical equilibrium assumption, the species molar composition at the wall  $\mathbf{X}_w$  can be computed from the local temperature  $T_w$ , pressure  $p_w$  and elemental molar composition  $\mathbf{X}_w^e$  by solving iteratively an algebraic system of equations [4, 25, 26]. In our implementation,  $p_w$  is extrapolated from the interior cell, whilst the wall temperature is calculated from the radiative equilibrium condition, as explained in the previous section. While in a full non-catalytic case, the heating due to gas convection is null, i.e.  $q_g^{conv} = \sum_s^{N_s} h_s \mathbf{J}_s \cdot \mathbf{n}_w = 0$ , if we assume local equilibrium at the wall, this term plays a role, since the gradient of species fractions across the wall is not null and contributes to increase the heat flux similarly to a full catalytic condition.

**Catalytic wall with finite rate chemistry.** A catalytic wall promotes recombination of atoms through exothermic reactions. For this reason it is very important to account for this phenomenon. On a partially catalytic wall we need to impose the molar fraction  $x_i$  of every species  $i$  such that the balance between the diffusive flux and the production rate is respected. To do this we solve the following equation by a Newton Method:

$$J_i(x_{j=1, N_s}) = \dot{\omega}_i(x_{j=1, N_s}) \quad (45)$$

where  $J_i$  represents the diffusion flux of the species  $i$ ,  $\dot{\omega}_i$  the production rate, and  $N_s$  is the number of species considered. The diffusive fluxes are computed using Fick's law. In this case, the diffusive flux  $J_i$  is proportional to the spatial derivative of the molar fraction  $x_i$  of the species  $i$ :

$$J_i = \rho D^{Fick} \frac{\partial x_i}{\partial x} \quad (46)$$

In order to ensure the conservation of mass, the diffusive coefficient  $D^{Fick}$  of Fick's law is the same for all species and it is defined by:

$$D^{Fick} = \frac{1 - y_i}{S}, \quad S = \sum_{j_s=0}^{N_s} \frac{x_{j_s}}{D_{ij_s}} \quad (47)$$

where  $y_i$  is the mass fraction of an arbitrary species and the  $D_{ij}$  are the binary diffusion coefficients. The wall rate production is defined by:

$$\dot{\omega}_i = \mathcal{M}_i^\downarrow \gamma_i \sum_r \nu(i, r) - \sum_j \sum_r \gamma_j \mathcal{M}_j^\downarrow \mu(j, i, r) \quad (48)$$

where  $(\gamma_i)_{i \in [0, N_s]}$  is the catalytic recombination factor that is identified by the experiments.  $\mathcal{M}_i^\downarrow$  is the impinging flux of species  $i$  on the wall and it is defined by:

$$\mathcal{M}_i^\downarrow = y_i \rho \sqrt{\frac{T_w R}{2\pi m_i}} \quad (49)$$

where  $T_w$  is the temperature of the wall and  $m_i$  is the molar mass of species  $i$ . Finally, matrices  $\nu$  and  $\mu$  define the recombination reactions that happen at the wall:

- $\nu(i, r) = 1$  if the species  $i$  is destroyed during the reaction  $r$
- $\mu(j, i, r) = 1$  when species  $j$  is destroyed during reaction  $r$  it produces species  $i$

### 2.1.5 Boundary conditions for ICP solver

**Symmetry axis.** The electric field has to vanish on the symmetry axis:

$$E_{p, Re} = E_{p, Im} = 0. \quad (50)$$

**2D boundary.** We use the following formula to compute  $E_p$

$$E_p = i\omega \frac{\mu_0}{2\pi} \sum_{i=1}^{cells} \sqrt{\frac{r_i}{r}} j_i S_i G(k_i) \quad (51)$$

where  $\omega$  is the angular frequency,  $\mu_0$  is the magnetic permeability of free space ;  $(r, z)$  are the coordinates of the point where the Electric Field is to be computed; the summation extend over the number of cells  $i$ ,  $(r_i, z_i)$  are the coordinates of the  $i^{th}$  element of the domain and  $S_i$  its area, and  $j_i$  is the current density in it. And  $G$  is defined by:

$$G(k) = \frac{(2 - k^2)K(k) - 2E(k)}{k} \quad k = \sqrt{\frac{4R_c r}{(R_c + r)^2 + (z - Z_c)^2}}$$

Where  $K(k)$  and  $E(k)$  are the complete elliptic integrals of the first and second kind.

**Distribution A: Approved for public release; distribution is unlimited.**

### 2.1.6 Implicit time integration

An implicit Backward Euler method is applied to Eqs. (30) in order to converge to steady state:

$$\frac{\mathbf{U}(\mathbf{P}) - \mathbf{U}(\mathbf{P}^n)}{\Delta t} + \mathbf{R}^{FV}(\mathbf{P}) = 0 = \tilde{\mathbf{R}}(\mathbf{P}) \quad (52)$$

where  $\tilde{\mathbf{R}}(\mathbf{P})$  is a *pseudo-steady* residual,  $\mathbf{U} = \mathbf{U}(\mathbf{P})$  an explicit analytical relation and the vector of natural variables  $\mathbf{P} = [\rho_s, \mathbf{v}, T, T_V]$ , in which the governing equations are *explicitly closed* and in which it is therefore convenient to store the solution vector. The application of a one step Newton method yields the following linear system:

$$\left[ \frac{\partial \tilde{\mathbf{R}}}{\partial \mathbf{P}}(\mathbf{P}^n) \right] \Delta \mathbf{P}^n = -\tilde{\mathbf{R}}(\mathbf{P}^n), \quad (53)$$

where the jacobian matrix  $\frac{\partial \tilde{\mathbf{R}}}{\partial \mathbf{P}}$  is computed numerically. The GMRES algorithm with an Additive Schwartz preconditioner serves to solve in parallel the corresponding linear systems arising from Newton linearizations. The solution update is also performed in primary variables.

## 3 Numerical results

### 3.1 ICP simulation

The first step of the project was to simulate the flow in the Plasmatron in order to provide the inflow data at the exit of the torch. The chosen test conditions correspond to a static pressure  $P_s = 2010$  and a plasma power of  $80kW$ . The boundary conditions are shown in Fig. 13.

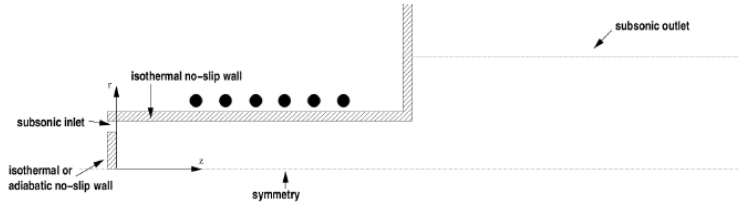


Figure 13: Setup of the boundary conditions for the ICP simulation.

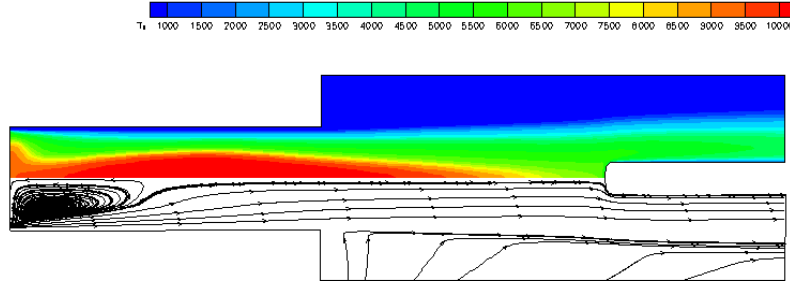


Figure 14: Temperature isolines (top) and stream lines (bottom) for the ICP simulation.

### 3.2 Nonequilibrium simulation

The focus of this project was to simulate a VKI Plasmatron experiment, including nonequilibrium and gas-surface interactions effects. The test consists in a plasma jet coming out from a ICP torch and impinging on a probe featuring different TPS materials. The actual TPS sample before the testing is shown in Fig. 15 and includes three patches with two different catalycities (low cat - high cat - low cat). The actual experiment is shown in Fig. 16: the test model, a flat plate probe with a blunted leading edge, is schematically depicted in Fig. 16(a), while Fig. 16(b) provides a infrared (IR) visualization of the temperature on the probe during the testing (courtesy from [27]). For our numerical investigation, the geometry has been assumed to be 2D, even though traditional effects cannot be excluded in the real case. A global and a detailed view of the 2D computational mesh used for this case are shown in Fig. 17(a) and Fig. 17(b) respectively. A refinement in the streamwise direction has been applied near the junctions between different materials in order to better capture the jumps in temperature and heating. A first cell size of  $10^{-5}$  [m] has been imposed close to the wall.

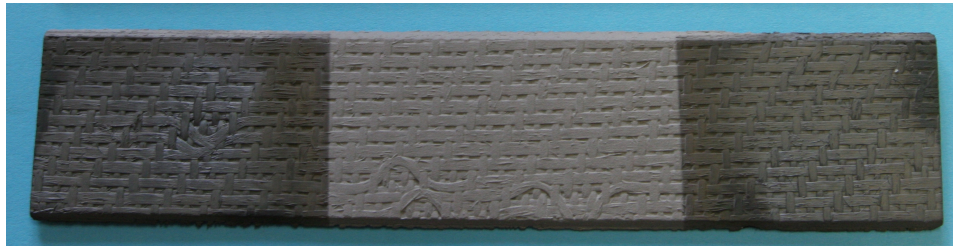
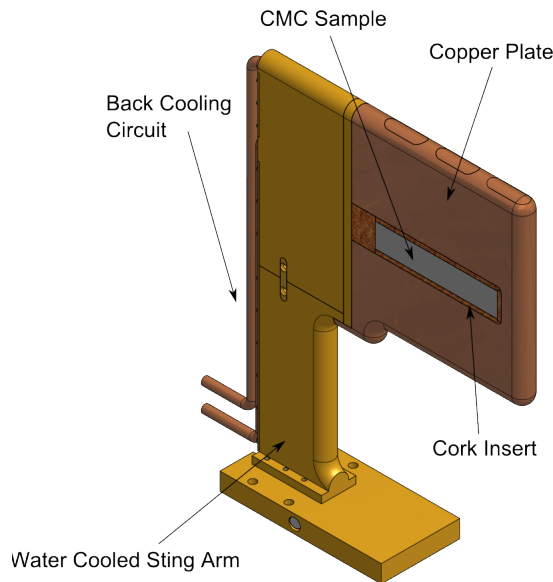
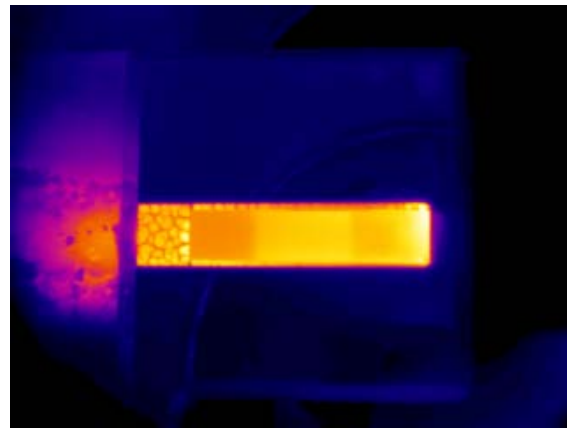


Figure 15: Three-patches TPS sample with two different catalycities [27].



(a) Flat plate probe configuration for TPS off-stagnation testing.



(b) IR visualization during actual testing on the flat plate probe.

Figure 16: Flat plate probe configuration and IR visualization during testing [27].

An axisymmetric ICP simulation of the full experiment (torch + chamber + test model) under a simplified LTE assumption (using the model detailed in Section 1.2) has provided the input jet profile for the nonequilibrium 2D calculation. In order to initialize the latter, the flow properties of the inlet subsonic plasma jet (in LTE conditions) have been extrapolated to all domain in the  $x$  direction. Herein, in order to stabilize the computation, an artificial blowing velocity  $u_x = 50$  [m/s] has been imposed in the inlet profile outside the jet, while  $u_y = 0$  [m/s] has been strongly set on the whole inlet boundary.

Following a conservative (probably even over-conservative) approach, the nonequilibrium calculation has been run in three steps using a limited second order scheme from the start:

1. At first, a fully adiabatic solution has been obtained starting from the previously described initial conditions.
2. Then, a solution with fixed temperature and radiative equilibrium on different wall patches has been computed.
3. Finally, the desired catalytic boundary conditions have been applied to the different wall patches, i.e. super-catalycity on the isothermal wall and the chosen partial-catalycity profile in combination with radiative equilibrium on the rest of the probe.

In the following, only the final solution is presented.

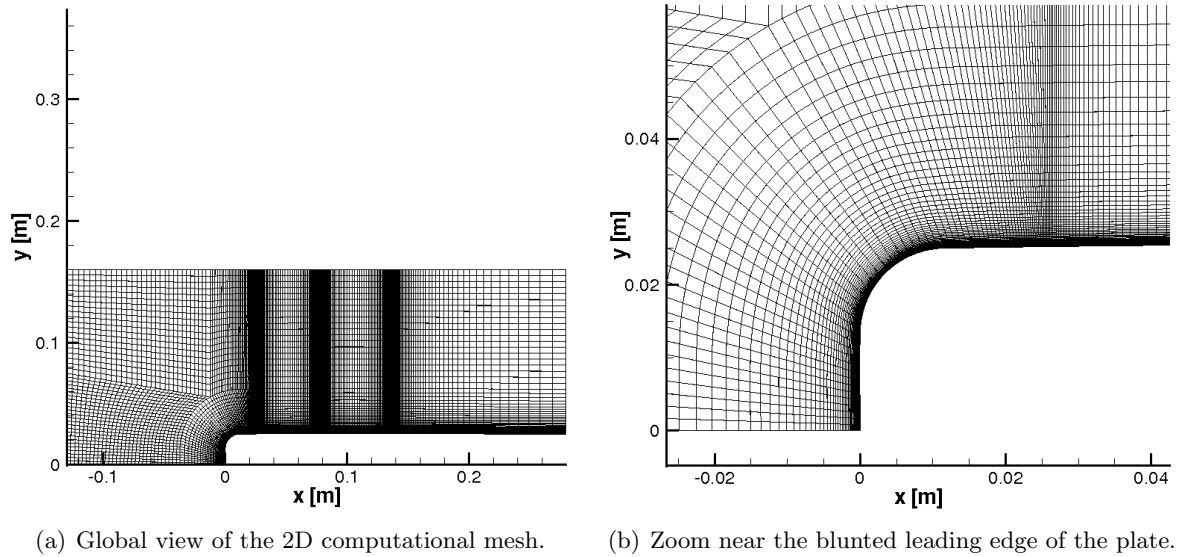


Figure 17: Views of the mesh (20450 cells) for the blunted plate.

A global view on the computed flowfield is presented in terms of temperatures and electron mass fraction. Roto-translational and (superimposed) vibrational temperature fields in Fig. 18 appear to be rather similar, which suggests that thermal nonequilibrium effects are playing a minor role in the flow. In particular, the flow appears to be in equilibrium close to the inlet boundary, which verifies a-posteriori the LTE assumption for the flow coming out from the plasma torch. Figure 19 shows that only the core of the jet, where temperatures reach up to 8000 [K], is characterized by ionized flow.

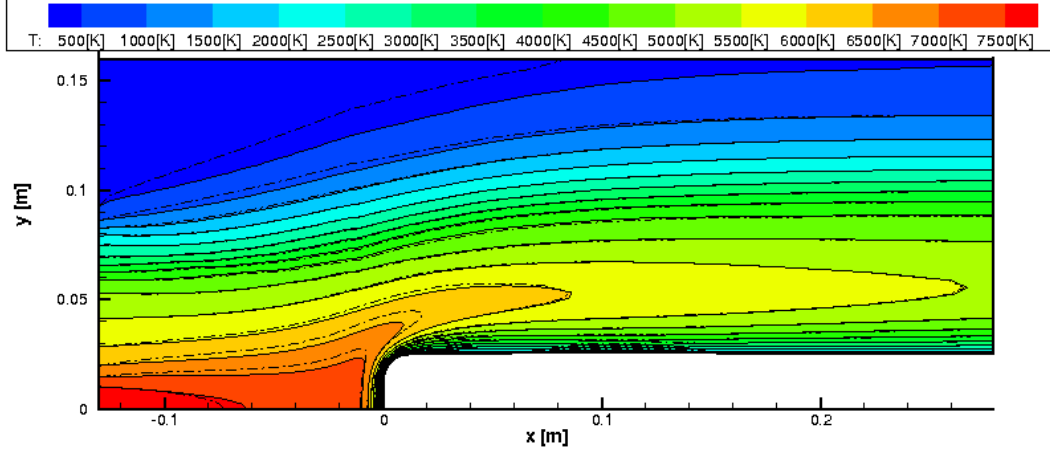


Figure 18: Roto-translational (contours, solid isolines) and superimposed vibrational temperature (dash-dot isolines).

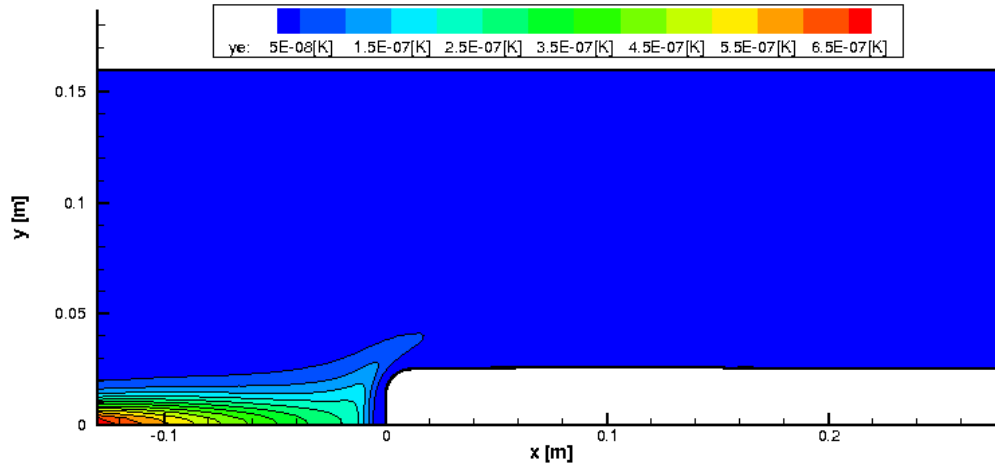


Figure 19: Electron mass fraction field.

Figure 20 shows a comparison between numerical results computed with the two gradient calculation methods described in Section 2.1.2 in order to assess their influence on the surface temperature and heat flux distributions. Kim's method (indicated as *grad model 1*) tends to predict up to 3% higher temperature where radiative equilibrium is imposed at the wall and up to 7% higher heat flux along almost all the body. In particular, Kim's method predicts 1.19 versus 1.11 [MW/m<sup>2</sup>] peak heating on the blunted leading edge and 0.87 versus 0.82 [MW/m<sup>2</sup>] on the junction between low- and high-catalycity patches. The results here presented show a qualitative and quantitative behavior (particularly, in terms of heat flux distribution and peak values) consistent with the experimental measurements in [27], even though the conditions for the experimental setup do not fully match the simulated conditions. A more quantitative validation of the numerical results against available experimental data will be addressed in the future, after the inclusion of a more accurate diffusion model for characterizing wall catalycity.

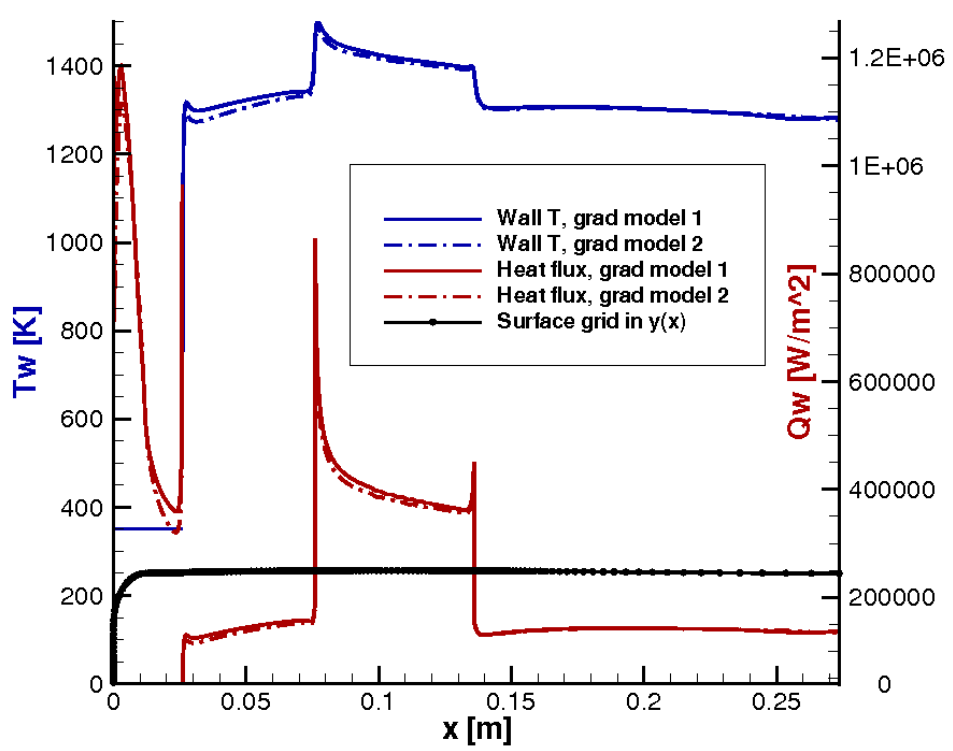


Figure 20: Surface distribution of temperature and heat flux along the plate computed with two different methods for gradient calculation: Kim's (grad model 1) and diamond (grad model 2).



## Part III

# Numerical simulation of plasma jet around the VKI rounded nose flat plate probe

## 1 Introduction

The aim of this contribution has been to compute the flowfield around the Von Karman Institute (VKI) rounded nose flat plate probe. The probe is conceived to simulate a vehicle off-stagnation region flowfield inside the VKI Plasmatron facility. The probe, shown in Fig. 21, consists of a copper plate with a 12.5 mm nose radius and can host a 152x30 mm rectangular insert at 26 mm distance from the leading edge [28]. The insert can be made of different materials; in Fig. 22 the low-high-low catalycity insert is shown. The high catalycity patch is realized by coating the sample with a Mullite section starting at 50 mm from the insert upstream edge and ending at 110 mm, the low catalycity part is made of SPS C/SiC [28].

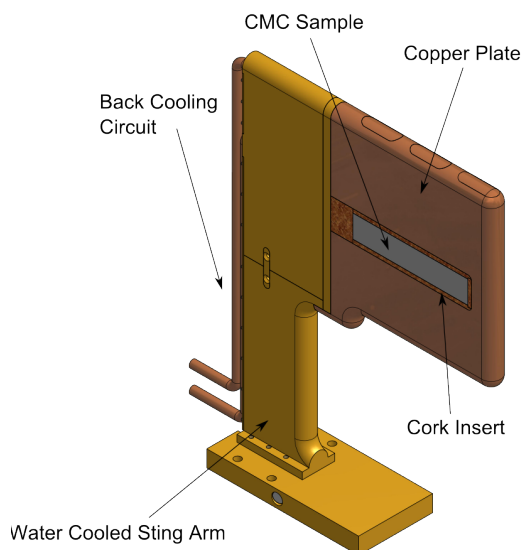


Figure 21: Flat plate probe configuration for off-stagnation testing.



Figure 22: Low-high-low catalycity insert.

The experiment for the flat plate probe has been carried out for a Plasmatron pressure chamber of 1500 Pa. The estimated enthalpy of the high temperature jet impinging on the probe is of  $19.8 MJ/kg$  [28]. The experimental values of surface temperature over the catalytic insert are shown in Fig. 23. The reported values are for three different insert, a low catalytic one, a high catalytic one and the low-high-low catalytic one of Fig.22. In Sec. 3 we will show the

computations performed, for the low-high-low insert, with the finite volume code Cosmic [29].

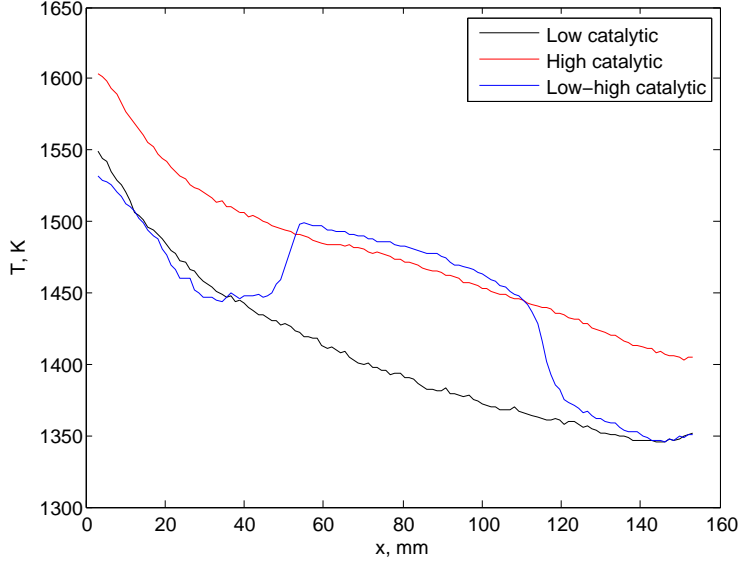


Figure 23: Experimentally measured temperature over catalytic insert.

## 2 Numerical model

The computations of the flow-field around the flat plate probe with the low-high-low catalytic insert have been performed with the code Cosmic [29]. Cosmic is a multiblock structured finite volume code able to deal with arbitrary mixtures of chemically reacting gases. The convective fluxes are discretized with the artificially upstream flux vector splitting (AUFS) scheme [30]. The scheme has been preconditioned by the author [31] and is able to compute flows over a wide Mach number range, from practically incompressible flow to hypersonic one. Diffusive fluxes (stress tensor, heat flux and species diffusion) are discretized with a central scheme [29]. The mixture thermodynamic and transport properties are computed with the PEGASE library [32]. The species diffusion fluxes are computed with the Stefan-Maxwell equations in order to ensure a correct computation of the heat flux load [33].

### 2.1 Boundary conditions

The flat plate probe wall is made, in the case under study, by three different materials: water cooled copper, the low catalycity material and the high catalycity material. In the latter two cases we can assume that the wall reaches radiative equilibrium.

Over the copper section the boundary condition for the energy equation is very simple: the wall temperature is assumed to be constant, because of the water cooling. Over the insert we assume radiative equilibrium and impose that the heat flux from the gas to the wall is balanced by the radiative heat flux lost by the wall.

$$-\lambda \nabla T \cdot \vec{n}_w + \sum_{i=1}^{N_s} h_i \vec{J}_i \cdot \vec{n}_w = \sigma \epsilon (T_w^4 - T_\infty^4) \quad (54)$$

Here  $\lambda$  is the gas thermal conductivity,  $N_s$  the number of species,  $vecJ_i$  the  $i$ -th species diffusion flux,  $\sigma$  the Stefan-Boltzmann constant,  $\epsilon$  the wall emissivity,  $\vec{n}_w$  the wall normal; here we have implicitly assumed that wall absorptivity is equal to wall emissivity. Eq. 54 is a non-linear equation that can be solved to determine the wall temperature  $T_w$ .

The species diffusion fluxes at the wall are themselves computed by the catalycity boundary condition: the net amount of species  $i$  produced or consumed by surface reactions ( $\dot{w}_{i,cat}$ ) has to be balanced by the diffusion flux of species  $i$  itself. Therefore the boundary condition is:

$$\vec{J}_{i,w} \cdot \vec{n}_w = \dot{w}_{i,cat} \quad (55)$$

The wall reaction rate  $\dot{w}_{i,cat}$  is computed as:

$$\dot{w}_{i,cat} = m_i \mathcal{M}_i^\downarrow \sum_{k=1}^{n_r} \nu_{ki} \gamma_k^i - \sum_{l=1}^{n_r} \sum_{j=1}^{N_s} \mu_{lj} \gamma_l^j m_j \mathcal{M}_j^\downarrow \quad (56)$$

Here  $n_r$  is the total number of wall reactions and  $\gamma_k^i$  the recombination probability of every wall reaction. The first term in the latter reaction rate expression describes the depletion of species  $i$  due to wall chemical reactions; the second term describes the creation of species  $i$  by wall reactions. The matrix  $\nu_k$  has entry  $(k, i)$  equal to one if the  $i^{th}$  species is destroyed in the  $k^{th}$  reaction, otherwise zero; the  $\mu_l$  matrix has entry  $(i, j)$  equal to one if the  $j^{th}$  species produces the  $i^{th}$  one in the  $l^{th}$  reaction, otherwise zero.  $\mathcal{M}_i^\downarrow$  be the number flux of species  $i$  impinging the surface and its expression, computed from the kinetic theory of gases, reads:

$$\mathcal{M}_i^\downarrow = n_i \sqrt{\frac{kT_w}{2\pi m_i}} \quad (57)$$

Our implementation of the catalycity boundary condition of Eq. 55 is based on the observation that, at the wall, the diffusion flux is already known and it is equal to the heterogeneous recombination rate  $\dot{w}_{i,cat}$ . The Stefan-Maxwell equations are multiplied by the normal to the wall and  $\dot{w}_{i,cat}$  is stuck in the equations, in this way they become a set of equations for the determination of the species chemical composition at the wall instead of species diffusion flux. This implementation of the boundary conditions has the advantage of being fully consistent with the model used to computed species diffusion fluxes in the bulk of the flow.

### 3 Results

We performed a series of computations of the flow field around the flat plate probe: our aim is to compare the computed wall temperature over the low-high-low catalytic insert with the experimental values [28]. The computational grid is shown in Fig. 24; as it can be noticed the grid covers only a part of the Plasmatron test chamber. VKI researchers provided us the relevant input conditions needed by the Cosmic code [34]: essentially the values of temperature and velocity on the left boundary of the computational domain, the chemical composition is assumed to be in chemical equilibrium at the inlet of the domain. This assumption is also made in the rebuilding procedure for the measurement of catalytic properties in the Plasmatron facility [35, 28]. The input values of temperature and horizontal component of velocity are shown in Fig. 25.

Due to the relatively low maximum temperature inside the plasma jet ( $T_{max} \approx 5800 K$ ) we used five species air ( $N_2$ ,  $O_2$ ,  $NO$ ,  $N$ ,  $O$ ) for the computations: the ionization level is not high

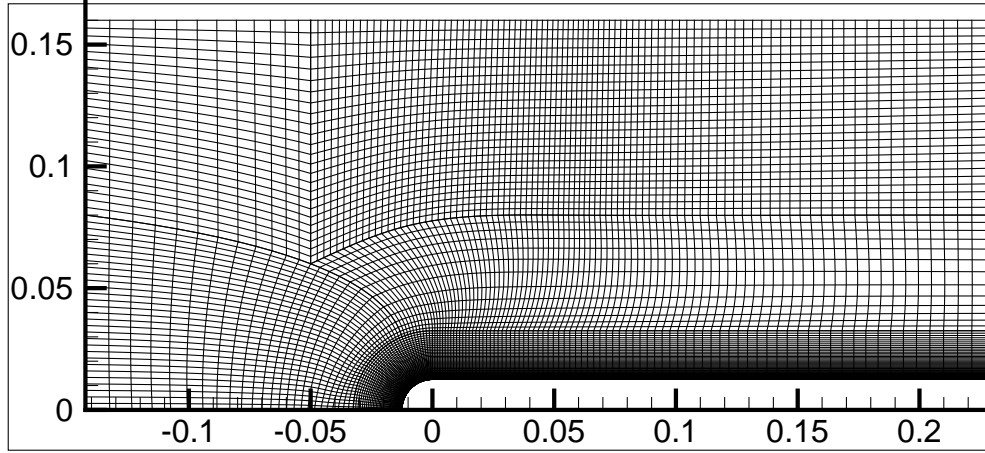


Figure 24: Computational grid.

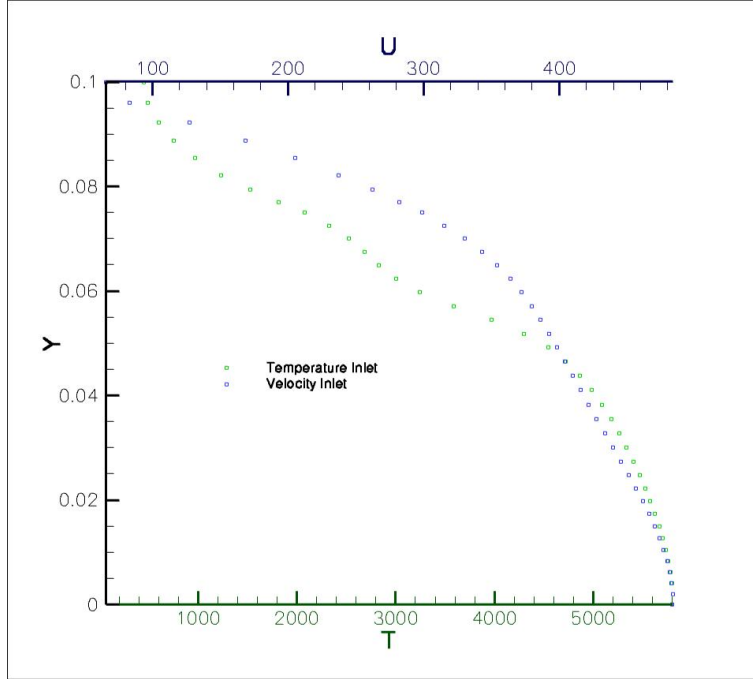


Figure 25: Input boundary conditions at 130 mm from probe leading edge.

enough to significantly affect the heat flux [29]. The reaction rate data of Park [36] were used for the chemical reactions inside the bulk of the flow.

At the wall we considered two possible catalytic reactions:  $N + N \rightarrow N_2$  and  $O + O \rightarrow O_2$ ; we assumed that the recombination probability  $\gamma$  is the same for both reactions. The values of the recombination rate probabilities for the three materials (copper, low-cat, high-cat) are shown in Table 3. We selected two different values of  $\gamma$  for the low catalytic insert to take into account the experimental uncertainties [28].

The wall temperature is imposed to be equal to 350 K on the copper cooled section of the probe, but it is computed from the radiative equilibrium condition on the catalytic insert; the wall emissivity is assumed to be equal to 0.85 for both low catalytic and high catalytic sections.

	copper	low-cat	high-cat
case c1	$\gamma = 1$	$\gamma = 0.012$	$\gamma = 0.06$
case c2	$\gamma = 1$	$\gamma = 0.008$	$\gamma = 0.06$

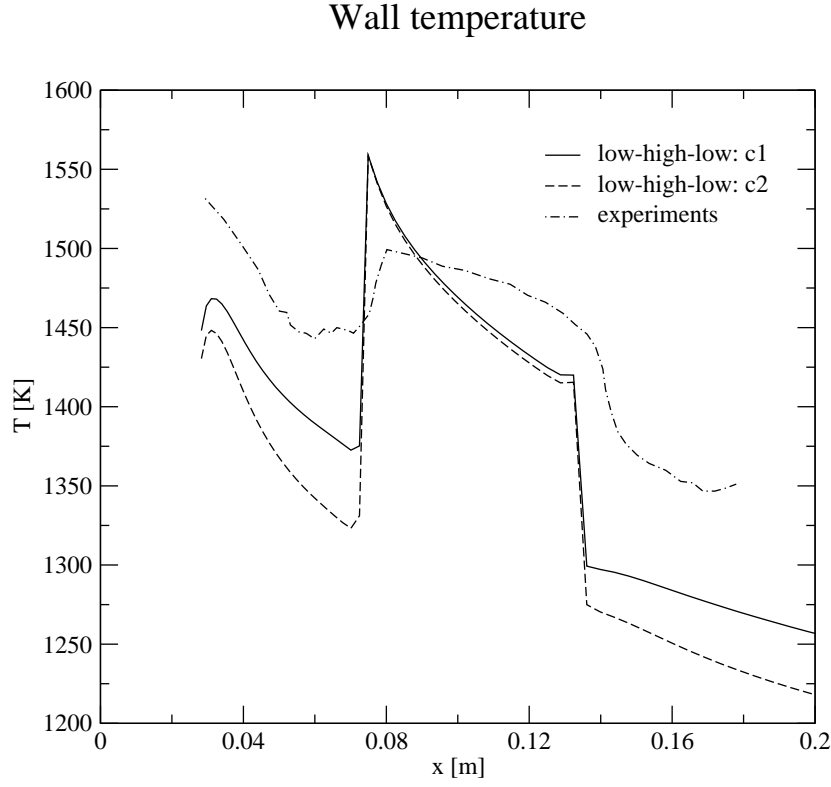


Figure 26: Wall temperature over the catalytic insert.

In Fig. 26 the computed wall temperature over the catalytic insert is shown, along with the experimental results. First of all we notice a non negligible difference in the temperature of the low catalytic insert between case *c1* and case *c2*, the temperature of the high catalyticity region being only marginally affected by the catalytic values of the previous section. We remark a decent qualitative agreement with the experiments, although the computed temperature of the low catalytic region is appreciable lower than the experimental one. On the opposite the computed and experimental temperatures of the high catalytic region show a better agreement.

## References

- [1] A. Lani, T. Quintino, D. Kimpe, H. Deconinck, S. Vandewalle, and S. Poedts. The COOLFluiD framework: Design solutions for high-performance object oriented scientific computing software. In P. M. A. Sloot V. S. Sunderan, G. D. van Albada and J. J. Dongarra, editors, *Computational Science ICCS 2005*, volume 1 of *LNCS 3514*, pages 281–286, Atlanta, GA, USA, May 2005. Emory University, Springer.
- [2] A. Lani, T. Quintino, D. Kimpe, H. Deconinck, S. Vandewalle, and S. Poedts. Reusable object-oriented solutions for numerical simulation of pdes in a high performance environment. *Scientific Programming. Special Edition on POOSC 2005*, 14(2):111–139, 2006.
- [3] T. Quintino. *A Component Environment for High-Performance Scientific Computing. Design and Implementation*. PhD thesis, Katholieke Universiteit Leuven, 2008.
- [4] Andrea Lani. *An Object Oriented and high performance platform for aerothermodynamics simulation*. PhD thesis, Université Libre de Bruxelles, Chaussée de Waterloo, 72, 1640 Rhode-St-Genèse, Belgium, 2008.
- [5] P. A. Gnoffo, R. N. Gupta, and J. L. Shinn. Conservation equations and physical models for hypersonic air flows in thermal and chemical non-equilibrium. Technical Paper 2867, NASA, 1989.
- [6] C. Park. *Nonequilibrium Hypersonic Aerothermodynamics*. John Wiley and Sons, New York, 1989.
- [7] G. Degrez T. E. Magin. Transport algorithms for partially ionized unmagnetized plasmas. *J. Comput. Phys.*, 198, 2004.
- [8] G. Degrez T. E. Magin. Transport algorithms for partially ionized unmagnetized plasmas. *Physical Review E*, 70, 2004.
- [9] D. Vanden Abeele. *An Efficient Computational Model for Inductively Coupled Air Plasma Flows under Thermal and Chemical Non-Equilibrium*. PhD thesis, Katholieke Universiteit Leuven, Chaussée de Waterloo, 72, 1640 Rhode-St-Genèse, Belgium, November 2000.
- [10] P. F. Barbante, G. Degrez, and G. S. R. Sarma. Computation of Nonequilibrium High-Temperature Axisymmetric Boundary-Layer Flows. *Journal of Thermophysics and Heat Transfer*, 16(4):490–497, 2002.
- [11] A. V. S. Prasad. *Numerical simulation of hypersonic flows and associated systems in chemical and thermal nonequilibrium*. PhD thesis, Dept. of Fluid Mechanics, Vrije Universiteit Brussel, Brussels, Belgium, Feb 1997.
- [12] C. Park. Problems of rate chemistry in the flight regimes of aeroassisted orbital transfer vehicles. Technical Paper 84-1730, AIAA, Snowmass, Colorado, June 1984.
- [13] J. D. Anderson. *Hypersonic and High Temperature Gas Dynamics*. McGraw-Hill, 1989.
- [14] R. C. Millikan and D. R. White. Systematics of vibrational relaxation. *Journal of Chemical Physics*, 39(12):3209–3213, 1963.

- [15] C. Park. Review of chemical-kinetic problems of future nasa mission, I: Earth entries. *Journal of Thermophysics and Transfer*, 7:385–398, July-Sept 1993.
- [16] M. Panesi. *Physical models for nonequilibrium plasma flow simulations at high speed re-entry conditions*. PhD thesis, Università di Pisa, Von Karman Institute of Fluid Dynamics, 2008.
- [17] K. Sutton and P. A. Gnoffo. Multi-component diffusion with application to computational aerothermodynamics. Technical Paper 98-2575, AIAA, Albuquerque, New Mexico, June 1998.
- [18] E. Sartori. Numerical simulation of chemical reactive flows in inductively coupled plasma windtunnels. Msc. thesis, University of Padua and von Karman Institute for Fluid Dynamics, 2009.
- [19] Timothy Barth. Aspects of unstructured grids and finite volume solvers for the euler and navier-stokes equations. 25th Computational Fluid Dynamics Lecture Series. Von Karman Institute, March 1994.
- [20] V. Venkatakrishnan. Convergence to steady state solutions of the euler equations on unstructured grids with limiters. *Journal of Computational Physics*, 118:120–130, 1995.
- [21] M. S. Liou. A sequel to ausm: Ausm+. *Journal of Computational Physics*, 129:363–382, 1996.
- [22] M. Delanaye, M. J. Aftosmis, M. J. Berger, Y. Liu, and T. Pulliam. Automatic hybrid-cartesian grid generation for high-reynolds number flows around complex geometries. In *AIAA Paper 99-0777*, Reno(NV), Jan 1999. 37th AIAA Aerospace Science Meeting and Exhibit.
- [23] Alpesh Patel. *Développement d'un solveur RANS adaptatif sur maillages non-structurés hexaédriques*. PhD thesis, Université Libre de Bruxelles, Faculté des Sciences Appliquées, February 2003.
- [24] B. Makarov S.E. Kim and D. Caraeni. Multi-dimensional linear reconstruction scheme for arbitrary unstructured mesh. Technical Paper 2003-3990, AIAA, June 2003.
- [25] T. Magin. A model for inductive plasma wind tunnels. Ph.d. thesis, von Karman Institute for Fluid Dynamics, St.-Genesius-Rode, Belgium, June 2004.
- [26] D. Vanden Abeele P. Rini and G. Degrez. Closed form for the equations of chemically reacting flows under local thermodynamic equilibrium. *Physical Review E*, 72(011204), 2005.
- [27] F. Panerai. *Aerothermochemistry characterization of Thermal Protection Systems*. PhD thesis, Università degli Studi di Perugia and von Karman Institute for Fluid Dynamics.
- [28] F. Panerai. *Aerothermochemistry Characterization of Thermal Protection Systems*. PhD thesis, von Karman Institute, Belgium, 2011.
- [29] P. F. Barbante. *Accurate and Efficient Modeling of High Temperature Nonequilibrium Air Flows*. PhD thesis, Université Libre de Bruxelles-von Karman Institute, Bruxelles, Belgium, 2001.

- [30] M. Sun and K. Takayama. An artificially upstream flux vector splitting scheme for the Euler equations. *J. of Comp. Phys.*, 189:305–329, 2003.
- [31] P.F. Barbante. AUFVS-P: a robust all Mach number finite volume scheme for Euler and Navier-Stokes equations. Unpublished.
- [32] B. Bottin, D. Vanden Abeele, M. Carbonaro, G. Degrez, and G. S. R. Sarma. Thermodynamic and Transport Properties for Inductive Plasma Modeling. *Journal of Thermophysics and Heat Transfer*, 13(3):343–350, 1999.
- [33] P.F. Barbante. How diffusion modeling affects prediction of heat flux loads. Sixth European Symposium on Aerothermodynamics for Space Vehicles, 3-6 November 2008.
- [34] F. Panerai. private communication.
- [35] G. Degrez, P. F. Barbante, M. de la Llave Plata, T. Magin, and O. Chazot. Determination of the Catalytic Properties of TPS Materials in the VKI ICP Facilities. In *ECCOMAS Computational Fluid Dynamics Conference*. Swansea UK, September 2001.
- [36] C. Park. Review of Chemical-Kinetics Problems of Future NASA Missions, I: Earth Entries. *J. of Thermophysics and Heat Transfer*, 7(3):385–398, 1993.